Characterization of Fiber-Forming Peptides and Proteins by Means of Atomic Force Microscopy

Rhiannon G. Creasey[1], Christopher T. Gibson[1], and Nicolas H. Voelcker[2]

[1] School of Chemical and Physical Sciences, Flinders University, Bedford Park, SA 5042, Australia
[2.] Mawson Institute, University of South Australia, Mawson Lakes, SA 5095, Australia

* Corresponding author: Nicolas H. Voelcker, nico.voelcker@unisa.edu.au

Abstract

The atomic force microscope (AFM) is widely used in biological sciences due to its ability to perform imaging experiments at high resolution in a physiological environment, without special sample preparation such as fixation or staining. AFM is unique, in that it allows single molecule information of mechanical properties and molecular recognition to be gathered.

This review sets out to identify methodological applications of AFM for characterization of fiber-forming proteins and peptides. The basics of AFM operation are detailed, with in-depth information for any life scientist to get a grasp on AFM capabilities. It also briefly describes antibody recognition imaging and mapping of nanomechanical properties on biological samples.

Subsequently, examples of AFM application to fiber-forming natural proteins, and fiber-forming synthetic peptides are given. Here, AFM is used primarily for structural characterization of fibers in combination with other techniques, such as circular dichroism and fluorescence spectroscopy. More recent developments in antibody recognition imaging to identify constituents of protein fibers formed in human disease are explored.

This review, as a whole, seeks to encourage the life scientists dealing with protein aggregation phenomena to consider AFM as a part of their research toolkit, by highlighting the manifold capabilities of this technique.

Keywords

Atomic force microscopy, antibody-recognition imaging, protein aggregation, peptide fibers

1. Atomic Force Microscopy (AFM)

AFM is a scanning probe technique developed by Binnig *et al.*[1]. The technique relies on the piezo-driven movement of a sharp probe tip across a sample surface, generating deflections in the cantilever attached to the probe. These deflections for each x,y pixel on the scanned area are then generated into a topographical map. Because this microscope does not rely on light or electron beams as optical and electron microscopes do, resolution in AFM is not limited by diffraction, and true 3D information can be gathered (Table 1) [2]. Furthermore, the AFM does not require a vacuum to function effectively and can therefore be operated under a variety of environments, including liquid and in particular aqueous milieu (Table 1) [3]. Consequently, the AFM has become an invaluable tool for the life scientist interested in surface investigations at the nanoscale [3-10]. In particular, the biophysical characterization of proteins benefits from access to AFM-related techniques.

Table **1**.Brief comparison of microscopy techniques for characterizing single proteins.

	Electron Microscopy		**Optical Microscopy**		**Atomic Force Microscopy**
	Scanning	Transmission	Brightfield	Fluorescence	
Lateral Resolution	<1 nm	<1 nm	200 nm	200 nm	<1 nm
Structural Information	✔	✔	X	X	✔
Mechanical Information	X	X	X	X	✔
Physiological Conditions	X	X	✔	✔	✔
Molecular Recognition	✔	✔	✔	✔	✔
3D Information	✔^	X	X	X	✔

^ qualitative only

1.1 AFM Operation

The most common AFM setup utilizes an optical detection system [8]. A laser is aimed at the end of a cantilever where the probe tip is mounted (Figure 1). This laser reflects onto a position-sensitive photodiode, typically consisting of four quadrants. As the cantilever deflects due to the probe's interaction with the surface, the photodiode signal due to the laser spot in each quadrant will change. This change is monitored by the controller. The movement of the cantilever is calculated from the change in voltage of the photodiode. The cantilever or the surface itself can be moved with accuracy by a piezo scanner in 3D. Alternative detectors are available, based on optical interferometry, electrical capacitance, electron tunneling, and piezoelectric cantilevers [2]. However, due to the simple and robust operating principle of photodiode laser detection, alternative detectors are rare.

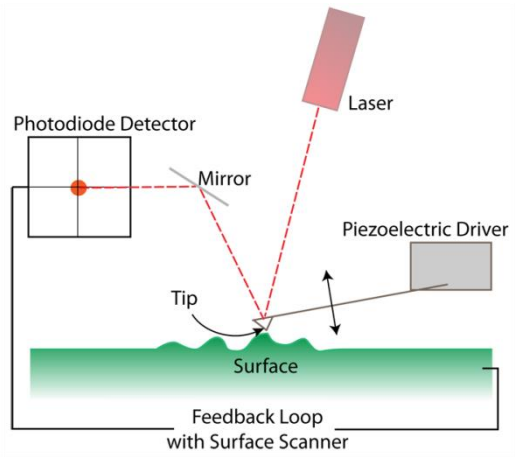

Figure 1 - Basic schematic of AFM operation showing laser-based detection of cantilever deflection.

1.1.1 AFM Imaging

1.1.1.1 Contact Mode (CM)

There are various modes of operation available for imaging using an AFM [2], the simplest being CM, where the probe is brought into contact with the surface, then 'dragged' laterally across the substrate. The force between the cantilever and the surface is maintained by keeping the deflection (setpoint) of the cantilever constant. In addition to topographical information, CM also provides frictional information as the probe 'drags' more heavily on areas of high friction and is subjected to torsional effects, which can be detected by the position-sensitive detector. In CM imaging, three basic channels of information can be acquired during the imaging process: height, deflection, and friction. The height image represents the true topography of the sample, converted from the movement of the piezo as it maintains the deflection setpoint. Typically, the z-height scale is represented as a color bar, where the colors of the pixels in the height image represent different physical heights.

When imaging, the setpoint is subtracted from the photodiode reading and this deviation is known as the 'error-signal'. This signal can be optimized in order to be quite large on steep gradients, but minimized on flatter areas. By mapping the cantilever deflection directly, the finer details of a surface can become visible in the 'deflection channel'. In this way, coarse details on rough samples can be sacrificed in order to visualize fine surface details. However, the z-scale in these images is not representative of true topography.

Finally, the friction channel records horizontal deflections of the cantilever. As the probe maintains constant contact with the surface, a higher friction between the probe and surface will result in increased torsional twisting of the cantilever, measured by the lateral photodiode quadrants. To avoid topographical artifacts, the comparison of topographic and lateral force images acquired in the same direction can be performed. A more common method seen is the subtraction of the forward and backward scanning direction from each other. However, correction for the nonlinear behavior of the piezoelectric transducer must be taken into account [11].

1.1.1.2 Intermittent and Non-Contact Modes

In tapping mode (TM) [12], the cantilever is oscillated near resonant frequency, and one of the components of oscillation, such as amplitude, is monitored for changes due to surface interactions. This mode of operation reduces the chances of damaging the probe or the surface, as the probe is in only intermittent contact with the surface. In TM imaging, three basic channels of information can be acquired while imaging: height, amplitude error, and phase. As with CM imaging, the height image represents the true topography of the image. Further, the amplitude error maps the 'error-signal' of the amplitude oscillation adjustments as a voltage from the photodiode measurements [2,12,13]. This channel can be equated to CM's deflection, and is useful for observing finer details on rough samples.

The phase channel essentially produces a map of how the probe interacts with the surface [2,12,14,15]. The phase lag of the probe's oscillation is measured with reference to the excitation oscillatory signal while the amplitude is maintained at a constant value. There are a variety of physical interactions that may cause the phase lag of the probe, such as surface stiffness, viscoelasticity and adhesion. Large topographical variations will also cause a phase lag. Phase imaging may provide further structural or compositional information than can be derived from a topography image of a substrate. However, interpretation of the phase signal is not straightforward and care must be taken when analyzing phase images.

These modes are by no means the only imaging modes. Non-contact AFM, for example, was the first AFM mode to provide atomic resolution on a silicon surface. In this mode, the probe never contacts the surface as it oscillates, avoiding sample or tip deformations [16,17]. The mapping of physical properties (based upon force spectroscopy, described in Section 1.1.2) is also available [2,12,18]. Furthermore, within each mode are alternative methods of cantilever excitation and detection, leading to a vast array of methods of extracting information from samples using AFM. Nevertheless, due to the gentle yet robust operational characteristics of TM, this mode is generally employed for initial investigations into biological surfaces [2,5,10,19].

1.1.2 Force Spectroscopy

Force spectroscopy is an AFM-based technique in which nanomechanical information can be obtained on the sample (Table 1) [20,21]. After positioning the AFM probe to the desired x,y position, the probe is brought into contact with the surface using the z-piezo, until the cantilever deflects, and it is then pulled away again. The cantilever deflection is graphed against the position of the z-axis, as seen in Figure 2.

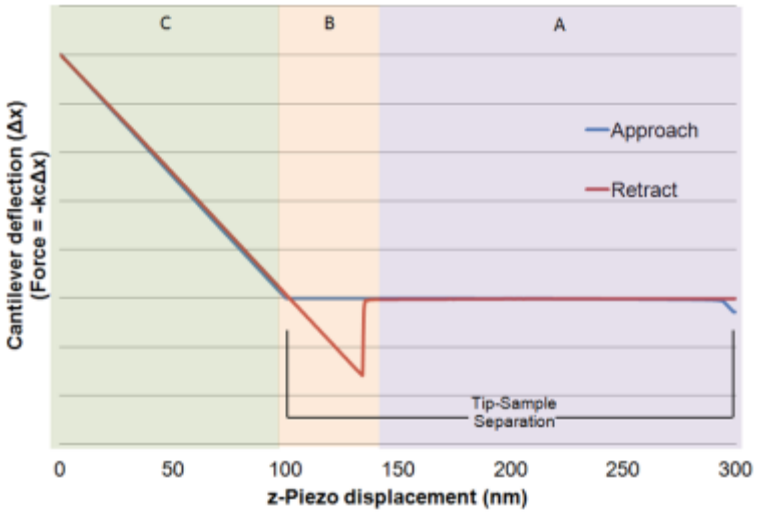

Figure 2 - A typical deflection *vs*. z-piezo displacement curve, tracking the deflection of a cantilever as it approaches towards (blue line) and retracts from (red line) a surface. In Region A, no deflection occurs. In Region B, the probe adheres to the surface on retraction and in Region C the probe is in contact with surface and the cantilever deflects upon further approach.

Initially, there are no forces acting on the cantilever, as it is too distant from the surface (Region A). As the probe approaches the surface, the atoms of the probe will interact with the atoms on the surface to create either an attractive or repulsive force due to van der Waals and electrostatic interactions in Region B. There is often a 'snap-on' effect seen when approaching in Region B, where the probe becomes close enough to the surface to be attracted by van der Waals forces [22]. In Region C, the probe is in contact with the surface, causing the cantilever to bend away from the surface due to the repulsive force of the electron orbital overlap between probe and sample. Sample and probe may undergo elastic and/or plastic deformations at this time, providing nanomechanical information of the surface. The cantilever is deflected up to a maximum loading value as set by the user, before reversing the z-direction to retract from the surface. When the probe is retracted (red line), adhesion between the probe and the surface often occurs, giving rise to a hysteresis effect (Region B). Finally, the probe 'snaps off' and loses contact with the surface (Region A).

If the properties of the cantilever are determined, then probe-sample forces can be quantitatively studied [23,24] on the basis of Hooke's Law (Equation 1).

Equation 1- Hooke's law of motion of a spring.

$$F = -k_c x$$

Where F is the force applied, x is the deflection of the cantilever, and k_c is its spring constant. Once the spring constant has been adequately calibrated (Section 1.1.2.1), the deflection-displacement curve can be converted to a force curve, in which the force applied to the cantilever is graphed against the probe's actual separation from the surface (tip-sample separation, denoted in Figure 2). Forces detected from the approach of a force curve include van der Waals, repulsive double-layer electrostatic, repulsive hydration, and the solvation forces. From the retract curve, the adhesion and hydrophobic forces between the probe and sample can be calculated [25]**.** As discussed above, the nanomechanical properties, such as stiffness (Young's modulus) of the sample, can be extrapolated from the contact forces (Region C) of a deflection-displacement curve. In the case of a probe indenting into the sample, the surface properties can be described by the Hertz model (Equation 2).

Equation 2 – Hertz equation of surface deformation.

$$F = \delta^{3/2} 2E \sqrt{\frac{R}{3(1-\upsilon^2)}}$$

Where δ is the indentation of the surface, E its Young's modulus, and υ is its Poisson's value, and R is the radius of the probe. However, this case does not take into account adhesion, which requires further calculations as provided by the Derjaguin–Müller–Toporov (DMT) [26,27] and Johnson–Kendall–Roberts (JKR) [28] theories

[29]. In biological samples, the surface is much softer than the probe, hence the JKR theory is usually applied for determination of sample deformation. The interested reader is referred to detailed reviews on the application of JKR and DMT theories [21,25,29,30]. However, state-of-the-art AFM instruments contain modules enabling the life scientist to easily measure surface stiffness, deformation and adhesion properties of biological samples. Some examples of force spectroscopy used for investigating fiber-forming peptides and proteins are included in Section 2.

1.1.2.1 Cantilever Calibration

The cantilever deflection can be measured with high precision using a position–sensitive photodiode. The calibration of the position-sensitive photodiode is usually done by performing force distance curves on a flat clean surface with a stiffness much greater than that of the cantilever. The average slope of the force distance curves, when the tip is in contact with the surface, will give the position-sensitive photodiode calibration factor or, as it is commonly known, sensitivity. For most AFM cantilevers, glass or silicon is sufficient. For stiffer cantilevers (with a stiffness greater than 100 N/m), sapphire may be more appropriate. Once the deflection of the cantilever is calibrated the spring constant must also be accurately determined. One of the earliest reliable methods utilised for the spring constant calibration of AFM cantilevers involved the addition of a known mass to a cantilever, resulting in a shift in the cantilever resonant frequency [31]. However, the addition of the mass, usually a small tungsten or gold sphere, is time consuming and potentially damaging to the cantilever and tip. Two non destructive and relatively simple methods are more commonly used for measuring the spring constants of AFM cantilevers; the so–called 'thermal method' and the 'Sader Hydrodynamic method'. The first derivation of the 'thermal method' was made by Hutter et al. [32] utilising the thermal fluctuations of the cantilever, relating the stiffness via the equipartition theorem, assuming the cantilever acts as a simple harmonic oscillator.

Equation 3 – Spring constant calibration using the 'thermal method'.

$$k_z = \frac{k_B T}{p}$$

where k_B is the Boltzmann constant, T is the temperature of the cantilever, and p is the area of the power spectrum of the thermal fluctuations (available experimentally). [33] Hence, this method is suitable to most AFM systems, as the temperature can be input easily and all other factors can be measured. However, the accuracy of this method is estimated to be between 10 – 20% [23], [34] due to the assumption that the cantilever acts as a perfect simple harmonic oscillator. A more accurate method reported to be as low as 5% [29], but usually closer to 10% [34] was developed by Sader et al. [35]. The 'Sader Hydrodynamic method' utilises precise measurements of the cantilever dimensions, Q factor and resonant frequency (f_r) and can be used for calibration of a cantilever in fluid.

Equation 4 – Spring constant calibration using the 'Sader method' for rectangular (k_{rect}) and 'V'-shaped (k_v) cantilevers.

$$k_{rect} = 0.1906\, lQ(\omega 2\pi f_r)^2 \rho_f \Gamma_i(v_k)$$
$$k_V = \frac{\epsilon \omega t_c^3}{2l^3}\, cos\alpha\, [1 + \frac{4\omega^3}{b_c^3}(3cos\alpha - 2)]^{-1}$$

Where Q is the quality factor of the cantilever, ρf is the density of the fluid the cantilever is immersed into, l and ω are the length and width of the cantilever respectively, and Γi is the imaginary part of the so-called 'hydrodynamic function'. This technique is only applicable to rectangular beam shaped cantilevers. Sader also derived an expression for V shaped cantilevers that is based on Euler beam equations [31] and is given in the second equation. In the second equation, the angle between the 'arms' of the V-shaped cantilever (α), the thickness of the cantilever (t_c),, the Young's modulus of the cantilever (E), and the base width of the cantilever (b_c) must be taken into account.

There are various calibration methods further to the ones discussed above [24,35], such as the use of reference cantilevers of measured dimensions, radiation pressure, capacitive sensors, and a differential pressure resulting from a known fluid flow rate [36]. The choice of which calibration method to use is not a trivial one. For most biological applications, the Sader or the thermal method are deemed adequate.

1.1.3 Probe Functionalization

Force spectroscopy can be utilized for molecular recognition, by attaching a ligand to a probe. Although molecular recognition is possible using immunorecognition by means of other microscopy methods (Table 1), force spectroscopy allows for true single molecule identification and measurement. Probe functionalization has

developed into a versatile procedure allowing hosts of ligands, including antibodies for specific molecular recognition to be attached to the probes without loss of biological activity [37-41]. Once an antibody is stably bound to the probe, force spectroscopy can be used to measure the specificity of the interaction of the corresponding protein. Data such as the binding kinetics, rupture forces and protein conformation [18,25,42-45] can be investigated. For more information on the use of functionalized probes in single molecule recognition force spectroscopy, reviews by Willemsen *et al.* [46], Leckband *et al.*[47], Kienberger *et al.*[48] and Hinterdorfer *et al.*[49] are recommended to the interested reader.

To functionalize a probe for molecular recognition, a biomolecule must be attached to the probe. This can be done via a linker, such as a biotin-streptavidin bridge [50-54], or glutaraldehyde crosslinking [55]. Alternatively, the biomolecule and the probe can be tethered via a defined covalent bond with a rupture force greater than the rupture force of the interaction being investigated [56]. This can be done using an amylose [56-59] or PEG chain [38,49,60-68] between an amine-reactive tip [69-73] and a biomolecule with available amino groups. A schematic used for linking antibodies to tips using a PEG linker is shown in Figure 3.

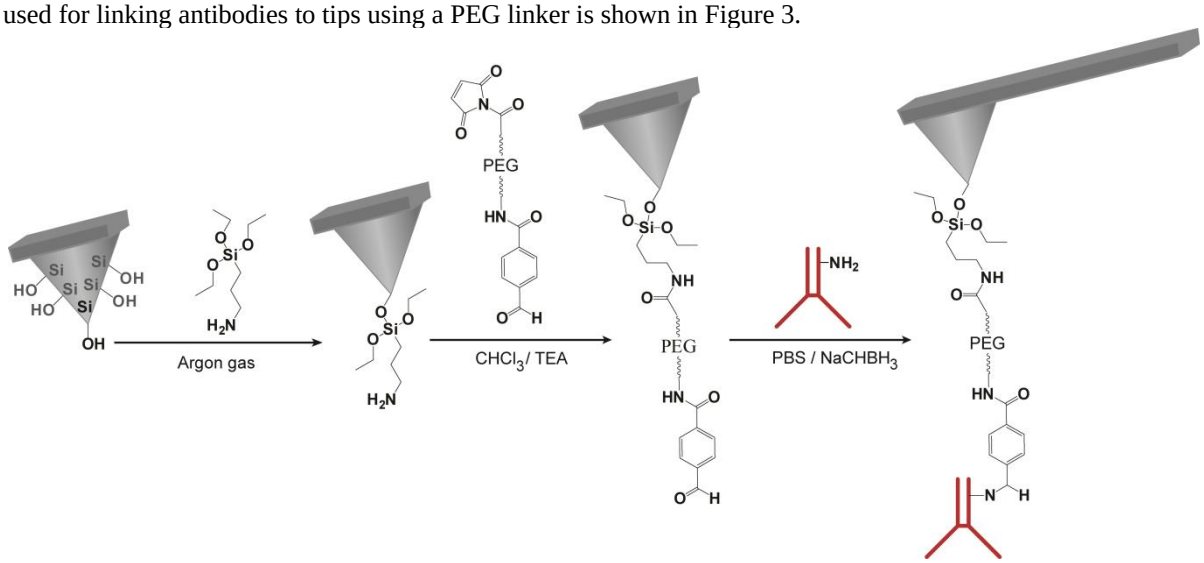

Figure 3 – A common coupling scheme for linking an antibody (red) to a 3-aminopropyltriethoxysilane-functional AFM tip (grey). After amine-functionalization, a poly-ethyleneglycol (PEG) chain is attached via its NHS-ester. The aldehyde residues on the free end of the PEG chain can be conjugated to the amino groups of the lysine residues of the protein. Reaction of antibody and aldehyde results in the formation of Schiff base, which is subsequently fixed by reduction with $NaCNBH_3$.

In the example in Figure 3, used for example by Chtcheglova *et al.*[74] and Creasey *et al.*[75], a probe is amine-functionalized using gas-phase silanisation with 3-aminopropyltriethoxysilane. An amide bond between the amine-activated tip and the activated carboxy group of an N-hydroxysuccinimide (NHS) ester end of a heterobifunctional aldehyde-PEG-NHS ester crosslinker is formed. Finally, the lysine residues of an antibody are coupled via the aldehyde residue of the crosslinker. Reduction with sodium cyanoborohydride stabilizes the Schiff base formed between the antibody and the aldehyde moiety. A variety of other chemistries are available for biomolecule immobilization on AFM tips. See also reviews by Ebner *et al.*[37] and Lee *et al.*[76], and a recent compilation of protocols published by Bergkvist and Cady [77], for in-depth information on probe functionalization.

1.1.4 Choice of AFM Probe

A critical parameter in any AFM measurements, regardless of mode, is the choice of cantilever and probe to be used. Several factors influence this decision such as the sharpness of the probe tip (its radius of curvature) determining lateral resolution, the aspect ratio of the tip, the cantilever spring constant (or stiffness), and cantilever reflectivity [2]. Due to tip convolution (discussed further in section 1.1.4), a sharp tip is generally preferred for imaging of samples [78]. However, for quantitative nanomechanical measurements of a surface, a nanoparticle attached to the tip is often employed [29] to provide a defined contact area, which is large enough to reduce the pressure and minimize damage to the sample. High-aspect ratio probes are required to image high-aspect ratio features on the sample. Harder silicon probes are employed for use in TM in air, and softer silicon nitride probes are employed for TM experiments in fluid or CM measurements. The cantilever and the tip are usually fabricated out of the same material. However, diamond tips [79] or carbon nanotubes [80] are at times mounted on silicon or silicon nitride cantilevers.

In CM imaging, due to the lateral motion of the probe, a V-shaped cantilever is preferred as it will have reduced torsional stress. In TM imaging, a rectangular cantilever is typically chosen which is oscillated at frequencies

above 50 kHz. This allows a minimum amount of force to be exerted on the sample to reduce deformation and damage, while keeping the probe stiff enough to prevent it from sticking to the surface due to capillary forces [2,12]. However when TM imaging in fluid, a softer V-shaped cantilever oscillating at a lower frequency of less than 20 kHz is typically employed as the fluid causes drag.
A highly reflective coating such as aluminum or gold may be used to ensure differentiation of reflection off the cantilever from reflection from the sample. In turn, magnetic coatings allow the cantilever to be driven magnetically. Magnet driving is suited for imaging in fluid, as the fluid is not disturbed by large oscillations due to acoustic drivers, and very small cantilever oscillations are possible to reduce the forces exerted on the sample [81].

1.1.5 Resolution

The z-resolution of the AFM is limited only by the electronic and thermal noise inherent in the cantilever detection system. 3D information in the range of Angstroms is typically achievable, and sub-Angstrom measurements can be realized on a well-calibrated instrument. Height measurements can be affected by adhesion and deformation, particularly when investigating biological samples [2,72,82]. Although a range of methods and calculations have been investigated for true height determination [12,24,83], TM employing minimal peak forces will minimize this deformation sufficiently for most investigations [12,83].
Lateral (x,y-plane) resolution is influenced by a range of factors. The tip's shape and size limit the geometrical topographies that can be observed due to 'convolution' [24]. As seen in Figure 4, a tip with an aspect ratio greater than the sample to be imaged will result in a 'broadening' artifact. This artifact is also observed if the tip is blunt or otherwise broadened due to contamination or damage.

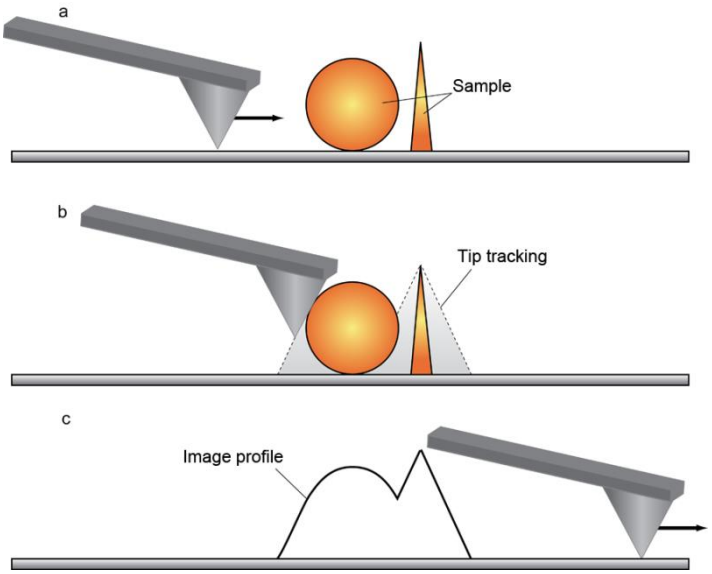

Figure 4 – 'Broadening' artifacts arising from tip convolution, where (a) shows the actual sample profile, (b) highlights the way the probe interacts with the sample resulting in (c) the line profile obtained.

It follows that the sample topography is also going to affect the imaging resolution, as regions which are inaccessible by the probe will not be visible. Furthermore, tip-sample interactions, such as long-range repulsive forces or sample deformation can also change the apparent features observed [84].
Such artifacts can be minimized by a judicious choice of probe (Section 1.1.3), and true surface features can be calculated by deconvolution algorithms. In this respect, the most accurate calculation is the Legendre function [85], which is, however, a rather cumbersome procedure. For most investigations, geometric deconvolution using the probe shape and radius of curvature is typically sufficient for determining true surface feature widths [86]. Determination of the probe's shape and radius of curvature can be done using a test sample surface of known geometries [87], available from most probe suppliers, and most commercial AFM software provides deconvolution packages.

1.2 Molecular Recognition Imaging

A further development of AFM, beyond morphology and mechanical characterization, is the so-called chemical force microscopy [88,89]. In this technique, the AFM probe displays certain chemical functionality or ligands to measure the interactions with molecules carrying functional groups or receptors on a surface. Probe

functionalization is discussed in Section 1.1.3, with reference to single molecule force spectroscopy. Here, probe-surface interactions are mapped to obtain information about the lateral distribution of molecular recognition events. Antibody functionalization of the probe is particularly popular for AFM based immunorecognition imaging or antibody recognition imaging.

A series of key developments have underpinned antibody recognition imaging at the nanoscale [49]. A comparison of the common antibody recognition imaging techniques is presented in Table 2. Phase imaging and force-volume imaging have been available for some years [12,51,90,91]. More recent developments, including HarmoniX™, PeakForce QNM™ (Quantitative Nanomechanical property Mapping) and picoTREC™ (simultaneous Topography and RECognition imaging; TREC), are also included [62,92-94].

Table **2**. Comparison of AFM techniques capable of antibody recognition imaging.

	Phase Imaging	**Force-Volume Imaging**	**HarmoniX™**	**PeakForce QNM™**	**PicoTREC™**
Real-time adhesion mapping	Yes	No (offline)	Yes	Yes	Yes
Proof of recognition specificity	Block	Force curve analysis / Block	Block	Block	Amplitude modulation / Block
Simultaneous topography and recognition	Yes	No	Yes	Yes	Yes
Lateral resolution	<5 nm	<100 nm	<5 nm	<5 nm	<5 nm
Ease of use / analysis	Easy / Moderate	Moderate / Moderate	Easy / Easy	Easy / Easy	Easy / Moderate
Specialized probes required	No	No	Yes	No	Yes
Time to obtain 1μm² image (512x512 pixels)	<5 min	>18 hrs	<5 min	<5 min	<5 min

The functionalization strategies and detection methods used in these areas have been extensively reviewed [7,37,49,95]. However, the following includes a brief review of the working principles of molecular recognition imaging and antibody recognition imaging in particular, and highlights some of the significant applications to biological sciences.

1.2.1 Force-volume Imaging

One of the features of force spectroscopy is that conformational changes of protein unfolding can be detected. The technique provides a platform for high throughput screening of environmental conditions [96,97] at which proteins may interact. Further, mechanical properties of cells and even cellular responses to physical stimuli can be investigated [98]. However, no information can be gained about the size and shape of potential aggregates, only the force of interaction between proteins, and structural changes resulting from these single molecule interactions. In order to compare the topographical features of a sample and localize the data obtained by force spectroscopy in the x-y axis, force-volume imaging was developed. By mapping the adhesion measured by force spectroscopy using a probe functionalized with antibodies or other proteins across a topographical area using force-volume imaging, the location and identity of proteins can be inferred at a sub-micron level. This method is inherently slow since each pixel requires a full force curve to be acquired. Furthermore, the CM image of the area must be acquired separately to the force curve. Over the timeframe of the experiment, drift in the x,y,z position is difficult to exclude, and this severely limits the resolution of the technique. Some offline calculations must be done to ensure the mapped adhesion is due to antibody recognition, and not due to non-specific interactions [99]. Additionally, a blocking step must be incorporated in order to reduce or eliminate signal due to receptor-ligand interactions, to prove molecular recognition specificity.

Dupres *et al*.[100] used a functionalized tip to map the adhesins on living bacterial cells using force-volume imaging. The blocking used in this experiment included addition of free heparin to block the surface sites of adhesin, shown by a reduction in binding events. This combination of force spectroscopy and adhesion imaging of the surface is a powerful technique, and has been applied to systems such as bacteria [101] and lipid membranes [102,103], among others [104,105]. The resolution of force-volume imaging is generally limited by the amount of time it takes to collect a force-distance curve at each point on the surface.

1.2.2 Phase Imaging

In TM imaging, the phase lag of the tip oscillation relative to the external driving oscillation can be monitored, as discussed in Section 1.1.1.2. A phase lag results from surface-dampened harmonic oscillations. This signal is

sensitive to short-range interactions such as adhesive forces and visco-elastic forces as well as long-range interactions such as magnetic and electric fields [12,15,91]. By utilizing a functionalized probe, the adhesion of the probe will be increased in areas where the corresponding ligand is located, resulting in increased phase contrast. However, due to the number of potential interactions leading to a phase response, it is difficult to map adhesion using solely this method. Li *et al.*[106] were able to identify angiotensin-II type 1 (AT1) receptors on a fixed neuronal membrane using an anti-AT1 antibody functionalized probe by employing 'interleaving' [107]. Interleaving involves scanning each line once in TM to detect topography, then again with a 'lift-up' to minimize surface contact for phase signal acquisition. Following data acquisition, a low-pass filter can be used to remove low-frequency topographical data from the phase channel. Interleaving has the disadvantage of increasing the image acquisition time. Furthermore, although interleaving can be used to separate the topographical information, the phase response may still be affected by other tip-sample interactions, and a blocking step as described for force-volume imaging should be applied for proof of specificity.

1.2.3 TREC

TREC operation relies on the use of a receptor-functionalized tip on a magnetic-coated cantilever oscillated by a magnetic field (Magnetic AC (MAC) mode). The receptor must be attached via a long, flexible crosslinker. As the receptor binds to ligands while imaging, this crosslinker will stretch during the 'upswing' of the oscillation, stunting the full amplitude. Meanwhile, the lower region of the oscillation is only affected by the sample topography. Hence, the probe oscillation trace is split into lower and upper regions with respect to the probe's resting position by the TREC equipment. Due to the nature of the data collection, TREC is capable of full-amplitude or half-amplitude feedback to eliminate topography signal from interfering in recognition data. Also, proof of recognition can be obtained without introduction of a free receptor or ligand by amplitude modulation inhibition of the crosslinker stretching [108].

TREC has been applied to a variety of biological systems, such as localization of streptavidin-based probes on bacterial S-layers [109], detection of human ergotoxin-1 on embryonic kidney cells [110] and recognition of cystic fibrosis transmembrane conductance regulator on human erythrocyte membranes [111]. Stroh *et al.*[62] analyzed lysozyme adsorbed on a surface using a HyHEL5 antibody-modified tip. Force curves were first obtained to confirm antibody specificity, before acquiring recognition images using both force-volume and TREC imaging (Figure 5).

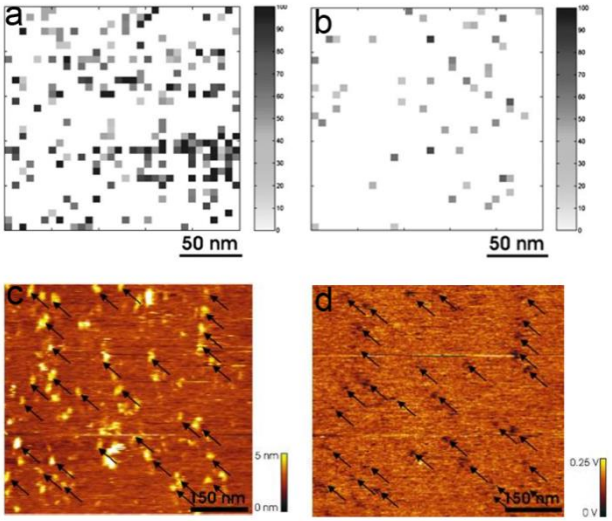

Figure 5 - (a, b) AFM force-volume images using lysozyme adsorbed onto a mica surface and HyHEL5 antibody attached to the probe. Binding sites on the lysozyme layer were detected in a, and blocked with free HyHEL5 antibody in solution in b. The unbinding forces in the pixels are scaled in gray scale values (0–100 pN). (c, d) Simultaneously acquired topography (c) and recognition (d) images using a HyHEL5 antibody-coated tip on mica surface with adsorbed lysozyme. The correlation between topography and recognition image is indicated with black arrows, showing that at least two-thirds of the lysozyme molecules are detected in the recognition image at the same position. Adapted from [62].

It is clear from Figure 5 that the resolution of TREC exceeds that of force-volume imaging. At the same scan size, whilst the force-volume image took 14 minutes at a resolution of 64 x 64 pixels, the TREC image was captured within 8 minutes at 512 x 512 pixel resolution.

Preiner *et al.*[108] investigated the optimal imaging conditions of TREC using a model protein interaction. Single avidin molecules were detected on mica using a biotinylated-IgG-functionalized tip. Minimization of topographical crosstalk was achieved by resonating the cantilever at a very low frequency. The modulation of the

amplitude of oscillation was investigated to determine the optical amplitude for a reliable recognition signal. The authors found that molecular recognition can be proven *in situ* by increasing the amplitude to a range higher than the crosslinker is capable of stretching. Blocking experiments as described for force-volume imaging that contaminate the tip and/or the sample are not required.
These examples of TREC imaging clearly demonstrate the usefulness of TREC to visualize, identify and quantify binding sites on biological surfaces. Comparison between the simultaneously acquired topography and recognition images yields high resolution maps, acquired in relatively short timeframes, on isolated proteins and fixed cell systems. TREC is still a relatively new technique, with continuing advances in methodology. The greatest advantage TREC has over other AFM antibody-recognition imaging is the ability to prove that adhesion is due to the antibody-mediated molecular recognition by modulating the amplitude of oscillation until crosslinker stretching is no longer causing a recognition signal [108]. This avoids contamination of the sample or the probe resulting from blocking experiments, and allows reuse of probe and sample.
Unfortunately, due to the need to use a long crosslinker, there is some lateral resolution loss due to tip broadening artifacts. Additionally, the use of specialized magnetically coated probes can increase the cost of running samples.

1.2.4 Other Molecular Recognition Techniques

PeakForce QNM™ is a recent technique developed by Bruker (previously Veeco) [93,94,112]. It utilizes a patent-pending algorithm designed specifically for the fast analysis of cantilever deflections when approaching and retracting from the surface. The instantaneous peak force is detected and minimized to avoid damaging the sample or probe, and calculations of the sample properties such as Young's modulus, deformation, dissipation and adhesion are *ad hoc*. Rico *et al*.[113] utilized PeakForce QNM to image the plasma membrane protein bacteriorhodopsin of *Helobacterium salinarum*, mapping the flexibility of membrane proteins at sub-molecular resolution. Stiffness measurements of the protein subunits were correlated with their secondary structures as shown in Figure 6.

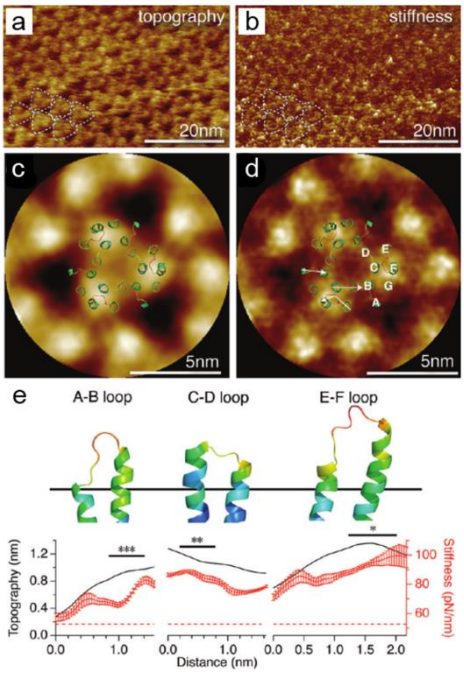

Figure 6 –PeakForce QNM images showing topography (a, z-axis = 1.5 nm) and stiffness (b, z-axis = 39 – 109 pN/nm) of bacteriorhodopsin protein layers, with individual trimers encircled in (c, z-axis = 1.5 nm) and (d, z-axis = 39 – 109 pN/nm). Individual loops are labeled. (e) Correlation of averaged topography and stiffness with loop structures calculated from 13 bacteriorhodopsin trimers from a and b and overlaid with the atomic structure [114]. Lateral view of the atomic structure colored by B-factors (top) of each cytoplasmic loop, and cross-sectional profiles (bottom) of topography (black) and stiffness (±standard error of the mean, red) along the arrows shown in d. The red dashed line shows the average stiffness of the lipidic region in d. Adapted with permission from [113].

By correlating the high resolution images seen in Figure 6 with mechanical maps, Rico *et al*. were able to identify which proteins contribute to structure and which contribute to function.
Another relevant technique recently developed by Bruker is HarmoniX™. This system utilizes specially designed 'hammer-head' shaped probes, oscillated at higher harmonic modes beyond the resonant frequency of the

cantilever. The torsional amplitudes are monitored, and the harmonics are converted back to the time domain to provide tapping force curves from lateral deflection signals. As the tip geometry and spring constant are known, maps of elasticity or adhesion can be extrapolated from the data [83]. To date, only two publications have utilized HarmoniX for biological applications. Husale *et al*.[115] imaged unlabeled DNA and RNA on a thiolated gold surface in order to determine the stiffness of single-stranded *versus* double-stranded molecules. The hybridized DNA strands were softer than their single stranded counterparts, double-stranded DNA having a stiffness of ~3.8 GPa compared with ~5 GPa for single-stranded DNA. Using these nanomechanical properties, it was possible to map the location of hybridized and un-hybridized DNA and RNA across a surface in a label-free manner.
Sweers *et al*.[93] used nanoindentation, HarmoniX and PeakForce QNM in their comparitive study of α-synuclein amyloid fibers. PeakForce QNM was able to gather mechanical data across the fibril images with more automation than nanoindentation, and less image artifacts than HarmoniX. The elastic modulus obtained by the three methods were corrected by accounting for the tip and fibril shape and size, and the values were comparable (1.3 – 2.1 GPa) for all techniques. Nanoindentation remains the most accurate method for biomechanical measurements at the nanoscale, but mapping techniques such as HarmoniX and PeakForce QNM are faster and simpler to use, and may consequently find application for screening purposes.
Adamcik *et al*.[94] applied PeakForce QNM to analyze the height, elastic modulus and deformation of amyloid fibrils from β–lactoglobulin (Figure 7), a protein present in milk which can form amyloid fibers under low pH and/or high temperature conditions.

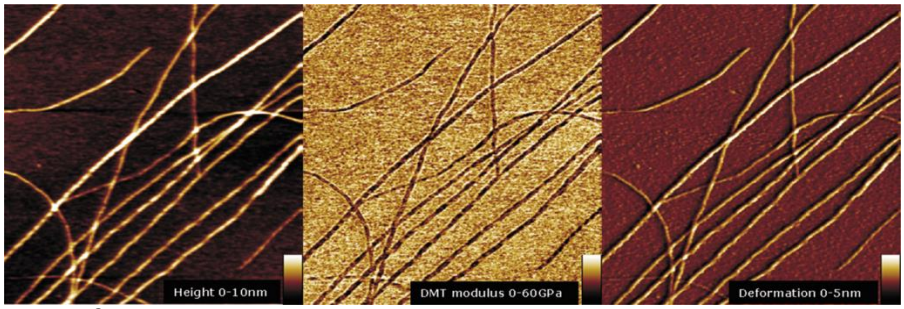

Figure 7 – 1.3 x 1.3 μm^2 AFM peakforce QNM images of β-lactoglobulin amyloid fibrils on mica. From left to right, data displayed are, respectively, topography (z-scale 10 nm), elasticity using a Derjaguin–Mueller–Toporov fit (z-scale 60 GPa), and deformation (z-scale 5 nm). Adapted with permission from [94].

The values found for elastic modulus of individual fibers supported indirect calculations by means of topological statistical analysis (utilizing polymer physics [116]) on fibrils structural conformations.
With the development of new AFM methodologies such as Peakforce QNM, nanomechanical data such as elasticity and deformation can be gathered quickly at the same time as morphological characterization.
To our knowledge, PeakForce QNM and HarmoniX have not been used for antibody recognition imaging in the literature. Antibody blocking would need to be carried out in order to prove antibody binding, contaminating the sample and probe. It would nevertheless be interesting to see how the results compare against TREC and other antibody recognition imaging techniques.

1.3 Combination with Non-AFM Techniques

Other microscopic (such as those seen in Table 1) or spectroscopic techniques can be combined with AFM on biological samples to acquire a more comprehensive understanding. Examples of relevant techniques that can be applied to samples prepared in parallel are circular dichroism (CD) spectroscopy for determination of protein secondary structure, dynamic light scattering (DLS) for determining size of proteins aggregates and fluorescence assays of fiber formation with Thioflavin T (ThT) and Congo Red (CR). Fluorescence microscopy can be combined with the AFM, as similar environmental conditions are achievable in both techniques. It is possible to attach a tip scanning AFM system on an inverted microscope to allow visualization of optically transparent samples, such as a monolayer of cells [117,118], or amyloid fibrils [119]. This combination of fluorescence microscopy and AFM has also been demonstrated for molecular recognition AFM. Duman *et al*.[120] have combined TREC imaging and fluorescence microscopy to determine density, distribution and localization of yellow fluorescent protein-labeled cluster of differentiation 1 molecules on α-galactosylceramide (*α*GalCer)-loaded human acute monocytic cells with a natural killer T-cell receptor modified AFM tip.
A variety of other techniques useful for investigating protein samples, such as Raman microscopy [121,122], and infrared microscopy [123], have also been coupled to AFM systems for simultaneous measurements of topography and chemical functional groups.

2. Fiber-Forming Peptides and Proteins

2.1 Protein Aggregation

Protein aggregation occurs when peptides or proteins assemble by being driven by non-covalent interactions into cluster of proteins, which will eventually phase-separate. Such aggregates can be amorphous, crystalline or have ordered superstructures such as filaments or fibers, and can occur in intra- and extracellular environments [124,125]. A typical protein folding pathway is shown in Figure 8, in which a native protein is partially misfolded, exposing regions which are normally hidden. These regions are often hydrophobic, driving aggregate formation in physiological environments due to the hydrophobic effect. In the schematic shown in Figure 8, there are four possibilities for the partially unfolded protein; it can revert to a native protein, completely unfold, or it can form aggregates [126,127].

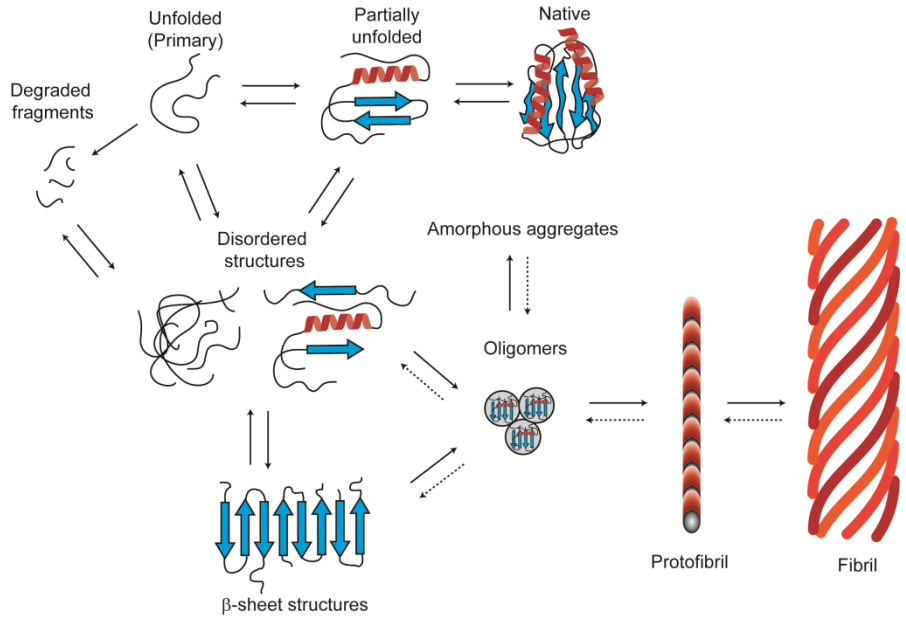

Figure 8 – Schematic of some of the many conformational states that can be adopted by polypeptide chains. All of these different conformational states and their interconversions are carefully regulated by the biological environment.

In general, fiber formation occurs via an aggregation pathway as in Figure 8. Peptide chain subunits fold into either disordered, partially ordered, or native states. These secondary structures may then assemble to form oligomers. After a nucleation event, elongation via the addition of further oligomers or monomers leads to the formation of protofibrils. It is generally agreed that the step at which protofibril growth from oligomers occurs is due to a nucleation event [128,129], and the time it takes for the nucleation event to occur is known as the lag phase or induction time. The nucleation step does not occur for all systems in which fibrils are formed from protofibrils; fibril formation can occur as a result of the breakdown and re-structuring of the protofibrils, or the bundling of multiple protofibrils [130,131]. In the literature, the nomenclature of fibrillar structures is not always clear; in this review, protofibrils refers to a fiber-like structure known to precede a fibril. Further ambiguity results from the use of the term, 'fiber,' which in common usage can refer to any elongated structure [132], and is often used interchangeably with 'fibril' in the literature. Again, for the purposes of this review, a fiber is considered the mature form of the protein or peptide aggregation, and may be formed of fibril subunits.

2.2 Amyloid Fibers

In terms of ordered protein aggregates, the most common form in nature is the group of amyloids. Amyloid deposits are implicated in over 40 different diseases, known collectively as amyloidoses. They also function in non-pathological roles, such as in spider silk [127]. These are polypeptide-based fibers characterized by a cross-β sheet structure as seen by X-ray diffraction, having a characteristic diffraction pattern with a sharp reflection at 4.7 Å along the same direction as the fiber, and a more diffuse reflection at between 10 and 11 Å perpendicular to the fiber direction [133]. Amyloid proteins do not necessarily share homology of peptide sequence, and it is the cross-β sheet conformation, which is the accepted biophysical hallmark of an amyloid fiber [134].

The mean aggregation properties and configuration of amyloid fibers have been studied using a variety of methods, including DLS, neutron scattering, CD spectroscopy, Fourier transform infrared (FTIR) spectroscopy, electron diffraction, electron paramagnetic resonance, and solid state nuclear magnetic resonance (ssNMR) [133,135]. Clinical diagnosis of amyloidosis, however, is usually carried out using a CR stain, by polarized

microscopy,or by immuno-gold EM, to detect amyloid plaques in tissue sections [127,134,136]. Amyloidic fibers display a range of ultrastructural polymorphisms, which are best investigated using high resolution microscopic techniques, such as AFM. Furthermore, high structural stability and resistance to degradation make these structures ideal candidates for nanomaterial design. It is therefore not surprising that peptides mimicking this aggregation pathway have also been extensively studied.
In the following two chapters, the use of AFM for morphological and mechanical characterization of amyloid fibers will be reviewed, with a focus on three disease-causing proteins; α-synuclein (αS), β-amyloids (Aβ) and prions.

αS is the main causative agent in the pathogenesis of Parkinson's disease [97]. The protein can form several aggregation states; these include a natively unfolded monomer, oligomers rich in β-sheets (protofibrils) and stable amyloids fibrils [137,138]. Amyloid structures interact with the neurons' cell membranes, resulting in destabilized cellular ionic homeostasis [139]. The AFM has been used to observe αS aggregation states, including non-fibrillar oligomers [140], spheroids, and fibril formation under a variety of conditions *in vitro* [141,142].
Aβ is a peptide of 39–43 amino acids that is processed from the so called amyloid precursor protein [143]. As the name implies, Aβ peptides form amyloidic rod-like fibers held together by β-sheets. The occurrence of Aβ fibrils, protofibrils and oligomers in amyloidic plaques within brain tissue is a hallmark of Alzheimer's disease [127,144]. Soluble Aβ peptide fragments found in cerebrospinal fluid from patients diagnosed with Alzheimer's disease are most commonly composed of amino acids 1 – 40 and 1 – 42 [145].
Prions are a unique form of infectious agent, consisting of misfolded proteins rather than organisms with a DNA/RNA code. The prions act as a template to induce the misfolding of normal proteins in neurological tissue, leading to amyloid inclusions [146]. Specifically, the cellular Prion Protein (PrP^{C}) is misfolded into an abnormal isoform (PrP^{SC}), which is insoluble and protease-resistant. PrP^{SC} is responsible for transmissible spongiform encephalopathies such as Scrapie and Creutzfeldt-Jakob syndrome, for which there is currently no effective treatment and which are invariably fatal [147].
As mentioned above, amyloid protein aggregates have become infamous for their involvement in neurodegenerative diseases such as Parkinson's and Alzheimer's disease [127,148], but are also implicated in a wide range of other disorders such as type II diabetes and cataracts [149, 150]. The reader is referred to an excellent in-depth review about protein misfolding in human disease by Chiti and Dobson [127].

2.2.1 Morphological Characterization of Amyloid Fibers

AFM offers a perspective on the mechanisms of assembly of amyloid fibers with nanoscale resolution under physiological conditions. Since the first papers to observe amyloid fibers by AFM in the 1990s, fibril growth and polymorphisms have been extensively investigated [138,151,152]. The ultrastructural characteristics of amyloid fibers, including the length and width, polymorphisms (curvature and persistence), periodicity and higher-order assembly have been described for amyloid fibers from a range of sources [116,132,133,152]. In general, amyloid fibers are observed to be long (up to several microns), straight and mostly unbranched. The diameter of the fibers varies between 5 – 25 nm [133,134] depending on the number of protofibrils twisted together to form a fibril. The fibril shape and contour depends on the number of protofibrils and overlapping β-sheets [87,133,134,144,153].
Stine *et al*.[151] observed Aβ(1-40) protofibrils using both CM and TM in air on mica and graphite. Protofibrils with an axial periodicity of around 25 nm were seen alongside smooth protofibrils of similar dimensions. The authors discuss some of the effects that sample compression and tip convolution can have on AFM measurements, and utilize both an internal calibration of plasmid DNA and an external calibration of Aβ measured by electron microscopy. Protofibrils were estimated to be 6 – 10 nm thick after taking into account AFM artifacts. These values are in the expected range for amyloid protofibrils.
Bocharova *et al*.[154] were able to induce PrP^{SC}–like aggregates from recombinant mouse full-length PrP^{C}. Anderson *et al*.[155] then used AFM and TEM to characterize the ultrastructure of the aggregated prion protein fibers. Interestingly, several different morphologies were observed based on AFM topography measurements. The major sub-types of polymorphisms identified were straight or slightly curvy ribbons, rod-shape protofibrils and bundles, protofibrils with a beaded nature, and ribbon-shaped protofibrils composed of laterally aligned sub-cords. Also described were protofibrils with a diverse range of twisting patterns, although these are far less commonly seen. The polymorphisms described were consistent with features seen in EM images of proteins isolated from Scrapie infected tissue, indicating that the PrP^{SC} are able to assemble into a certain range of conformations regardless of pathological *in vivo* or *in vitro* conditions. Petty *et al*.[156] synthesized peptide sequences based on the most amyloidogenic residues (109 – 122) of a prion protein found in healthy Syrian hamster. AFM imaging showed that modification of the amino acid present at residue 117 resulted in altered alignment of the peptides, either forming the long twisted rods expected of amyloid fibrils, producing smooth thin protofibrils, or preventing aggregation as seen for the wildtype PrP^{C}. This residue impacted on the assembly process of peptide fibers by

affecting the strand alignment and β-sheet crosslinking of adjacent peptides. Such studies may be useful in designing peptides or peptidomimetics to arrest prion aggregation.
Since the growth of fibrils is slow with respect to AFM imaging, time-lapse AFM can be used to observe the fibrillization process [157-159]. Goldsbury *et al*.[160] investigated the growth of Aβ(1-40) fibrils using TM AFM in neutral buffer (Figure 9).

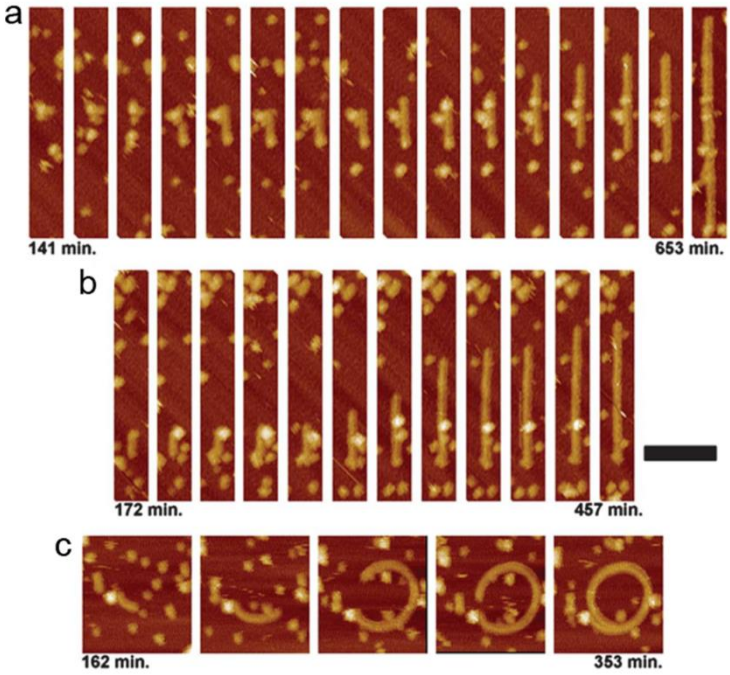

Figure 9 - Time-lapse (denoted beneath each image series) series of TM AFM height images showing protofibril elongation. Protofibril elongation was both bi-directional (a) and uni-directional ((b) and (c)).The scale bar = 200 nm. Adapted with permission from [160].

Monomers and high molecular weight oligomers were immediately observed on the mica surface, indicating the effectiveness of mica for adsorbing Aβ in fluid conditions. After 2 hours, protofibrils of width 6 ± 0.5 nm began to form on the surface. If Aβ fibrils were pre-adsorbed to mica instead of using clean mica, new protofibrils and oligomers were observed immediately, suggesting a seeding effect for pre-formed fibrils. As the Aβ peptide was consumed from solution by fibrillization, fibrils formed on the mica with heights of 10.7 ± 2.3 nm in two different discrete elongation steps: the first of which the authors interpret as the addition of protofibril subunits; the second possibly resulting from assembly of discrete independent peptides, morphologically resembling loosely twisted ribbons with ~80 – 130 axial cross-over spacings. Due to the constraints of fibril growth on surfaces, there may be additional pathways for fibril growth in solution which are not observed in this system.
Aβ(1-40) and Aβ(1-42) were also investigated using time-lapse AFM by Harper *et al*.[161] utilizing TM AFM in air. Here, Aβ(1-40)aggregation occurred within one week, yielding protofibrils of height 3.1 ± 0.3 nm. This time course was accelerated for Aβ(1-42), requiring only a day to form protofibrils of height 7.8 ± 0.5 nm. Over time, larger (at least double the height) fibrils appeared, effectively consuming the protofibrils (and not necessarily growing from them). Harper *et al*.[138] were able to speed up the growth of fibrils by adding pre-formed protofibril 'seeds'. The final fibers, consisting of a helical twisted structure, were compared with the fibers isolated from Alzheimer's tissue as well as other published amyloid fibers such as prions and found to have a similar morphology. This work demonstrated that the critical nucleation step is the transition from protofibril to fibril, and that seeding can effectively decrease the lag phase of fibril formation without affecting the final morphology.
The role of chaotropic denaturing agents in initiating amyloid fibril growth has been investigated by Polano *et al*.[162] who studied the aggregation of recombinant mouse prion protein (RecMoPrP(89-230)) previously shown to form prion fibrils when prepared in buffers containing guanidine hydrochloride (GdnHCl). GdnHCl is commonly used in diagnostic amyloid seeding assays [163,164]. At low concentration (0.4 M) of GdnHCl, only protofibrils or oligomers were observed by AFM. However, an increased concentration (2 M) led to the formation of amyloid fibrils as seen in Figure 10 below.

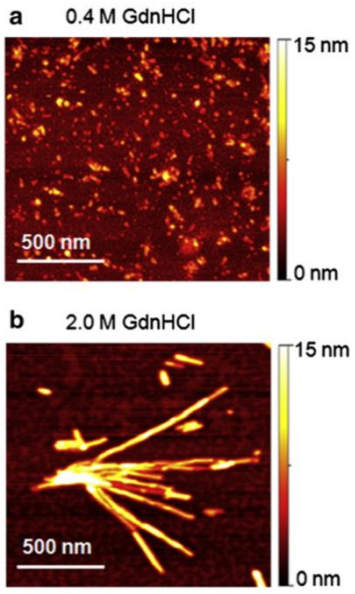

Figure 10 - AFM height mode images of prion aggregates formed in buffer containing 0.4 M GdnHCl (a) and 2.0 M GdnHCl (b). Adapted with permission from [162].

The nucleation event of aggregation of prion proteins into fibrils is affected by the hydrogen bond disrupting–GdnHCl, with an increased concentration of denaturing agent leading to the formation of more amyloid fibers. However, the ultrastructures observed by AFM at high concentrations of GdnHCl did not closely mimic those seen in purified disease prion aggregates. Instead of featuring many polymorphisms, like the PrPSC fibers from disease tissue, Polano observed a dominant morphology of rod-like fibers with height 5.7 nm (Figure 9), which indicated that this model system of aggregation may not reflect pathological conditions. Instead, Wegmann et al.[165] postulated that investigation of infected cells may reveal more relevant insights into the structure of prion proteins involved in disease pathology. In this study, AFM and light microscopy were used simultaneously on a culture of mouse neuroblastoma (N2a) cells infected with prions isolated from the brains of mice with Scrapie, as shown in Figure 11.

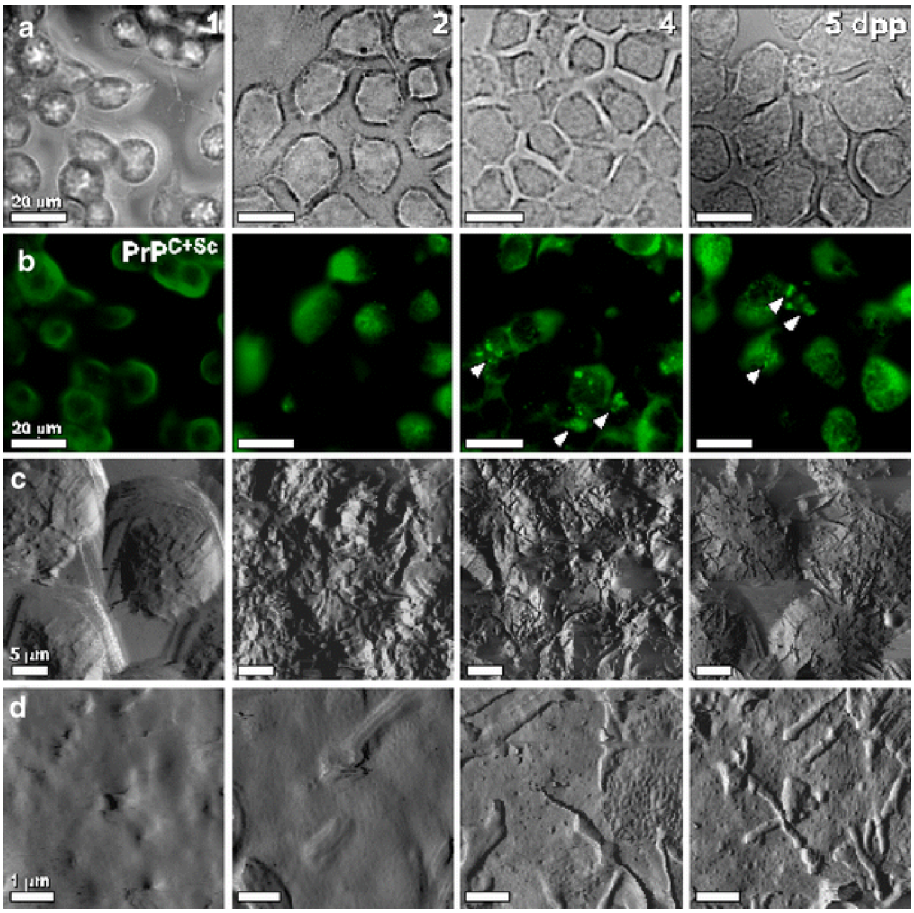

Figure 11 – Time course over 5 days, showing fibrillar surface structures on Scrapie-infected N2a cells (ScN2a) derived at 1, 2, 4 and 5 days after plating (columns). (a) Phase contrast microscopy images, and (b) immunofluorescence detection of Pr^{PC+Sc} with x-scale = 20 µm. (c and d) AFM deflection images of fixed ScN2a cells, showing an increase in fibrillar structures at 5 days after plating (c; x-scale = 5µm, and d; x-scale = 1 µm). Adapted from [165].

Immunofluorescence microscopy was used to identify infected cells, so that AFM could be applied on those as seen in Figure 10 to analyze structures on the cell surfaces. After 5-6 days, extensive fibrillar structures were observed, similar to those obtained from diseased tissue. Further investigations utilizing a cell culture system like that above could be used to investigate the environmental conditions of aggregation, and effectiveness of therapeutical drug targets.

Ku *et al*.[166] studied peptides based on one of the most amyloidogenic regions in the human prion protein (residues 106 – 127). Peptides were immobilized on NHS-ester activated glass or self-assembled monolayer-coated gold slides and analyzed by AFM and β-sheet binding dyes CR and ThT. Rod-like amyloid protofibrils formed from peptides in solution on these surfaces in more uniform morphologies and at a greatly increased rate compared to solution-based aggregation. This was thought to be due to the immobilized peptides having a seeding effect, rather than being a surface artifact. Although the system is arguably not the best mimic for the diseased state, it may nevertheless be useful for designing advanced diagnostic assays for disease detection. Also exploiting an NHS-ester surface, Ha and Park [167] immobilized Aβ monomers, oligomers and fully grown fibrils as seeds for Aβ(1-42) growth. Utilizing TM AFM in air, they studied the frequency and morphology of mature fibers. Pre-aggregated oligomers were found to be the most efficient at seeding by serving as a sink to soluble Aβ in solution. The use of functionalized surfaces for *ex situ* fiber formation is a highly effective method and reveals the effects of surfaces on amyloid aggregation. Further surface effects have been investigated as protein aggregation inducing factors. Giacomelli *et al*.[168] observed the influence of Teflon on Aβ fibril formation by inserting 100 nm Teflon nanoparticles into a solution of Aβ(1-40) peptide. Using a pH 10 buffer, Aβ was mostly observed as random coil and β-sheet structure in solution (by means of CD spectroscopy), converting to primarily α-helices upon introduction of Teflon particles. As the peptide concentration increased, β-sheet structures re-formed across the Teflon nanoparticle surfaces. Ideally, flat Teflon surfaces incubated with amyloid-forming peptides would be analyzed by AFM, since the morphology of the aggregates could then also be observed.

Zhu *et al*.[169] studied amyloidal fiber formation on mica since this is a commonly used ultraflat substrate for AFM studies. They observed that the lag phase for protofibril formation was shortened due to incubation in the

presence of mica, and protofibril formation occurred at lower concentrations, than incubation in the solution phase followed by deposition onto mica. Kowalewski and Holtzman [170] applied *in situ* TM AFM in pH 7.4 buffer to compare aggregation of Aβ(1-42) on mica and graphite. On mica, highly mobile globular aggregates of 5 nm height were observed with a tendency to coalesce to protofibrillar aggregates over a 20 minute period. In contrast, graphite was covered with elongated parallel sheet structures at 120° angles to each other within minutes of being introduced to the surface. These were interpreted as β-sheets, with extended peptide chains perpendicular to the long axis of the aggregates stabilized by the hydrophobic interactions between graphite and the peptides' hydrophobic residues. Wang *et al*.[171] observed a similar phenomenon for Aβ(1-42) peptides in a citrate buffer (pH 4) on a graphite surface. The authors also observed beaded protofibrils with a right-handed axial periodicity, for which self-assembly was suggested to be via a joining of bead-like aggregates, leading to elongated protofibrils of Aβ peptide, followed by the protofibrils intertwining into fibrils. This hydrophobically-driven self-assembly on graphite has also been observed by STM [172].

Gorman *et al*.[173] also investigated Aβ fibril formation on mica and graphite. Here, the shorter Aβ(1-40) peptide was used in a buffer of pH 6. Aggregation on mica was observed over a similar timeframe as described by Kowalewski and Holtzman [170]. However, large amorphous aggregates of 150 – 500 nm height were observed on the graphite surface. These large aggregates were transient, disappearing after longer incubation times. The main experimental differences between the work by Kowalewski and Holtzman and that of Gorman *et al*. are that Gorman *et al*. used a solution phase incubation before allowing aggregates to deposit onto the substrates, and that imaging was performed in air. Hence the differences observed between substrates by Gorman *et al*. are likely to reflect differences in the propensity of aggregates of varying hydrophobicities to adhere to the substrates, rather than result from surface-induced morphological differences on Aβ aggregation.

In order to observe the aggregation of amyloid fibers on more physiologically relevant substrates, solid supported lipid bilayer membranes have been employed. Quist *et al*.[139] monitored the interactions between amyloid forming proteins, including Aβ(1-40) and αS, reconstituted into 1,2-dioleoyl-sn-glycero-3-phosphocholine (DOPC) liposomes formed into lipid bilayers supported on mica. Individual pore-like structures were seen to form in the bilayer, with pores of 1 nm and 2 nm diameter, for αS and Aβ, respectively, which the authors suggest may support an ion channel function of the protein aggregates. Green *et al*.[174] also investigated Aβ(1-40) interactions with lipid bilayers of 1-palmitoyl-2-oleoyl-*sn*-glycero-3-phosphocholine (POPC) and 1-palmitoyl-2-oleoyl-*sn*-glycero-3-phosphoglycerol (POPG) (3:1) supported on mica in a pH 7.4 Tris buffer. In this case, pore-like structures were not observed, and instead the authors described expanding lesions caused by the adsorption of Aβ(1-40) to lipid bilayer defects. As the peptides were incubated onto the pre-formed lipid bilayers instead of being reconstituted into the liposomes prior to lipid bilayer formation, this suggests that the peptides do not span solid-supported lipid bilayers. Green *et al*. also suggest a toxicity mechanism for Aβ(1-40), but one involving membrane thinning rather than ion channel formation by protein aggregates. Indeed, the precursors of amyloid fibers are often identified as the cytotoxic element of amyloidosis [175-181]. Lowe *et al*.[182] have demonstrated that calcium and cobalt ions induce the formation of potentially pore-forming annular αS oligomers (Figure 12). The structure and properties of aggregation of αS in the presence of various metal ions is now well documented, with various mechanistic insights being provided [183,184].

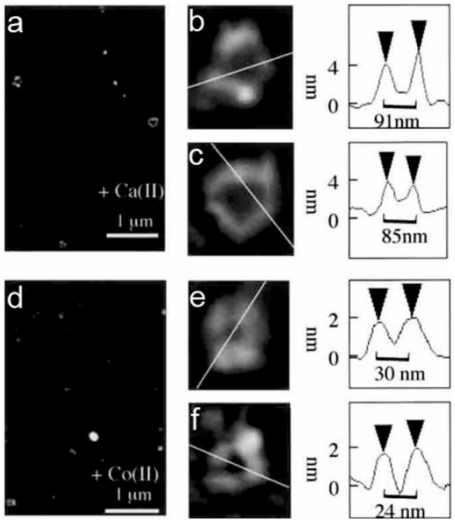

Figure 12 – TM AFM height images of αS annular particles, induced by the presence of calcium (a – c) and cobalt ions (d – f) after incubation at 4 °C for 1 day. Height cross-sections of αS particles are shown on the right. Adapted with permission from [182].

Pountney *et al.*[185] performed antibody recognition imaging utilizing a covalently bound organic crosslinker (trimethoxy-3-bromoacetamidopropylsilane) to functionalize the AFM probe with anti-αS antibodies. These probes were used to image annular nanoparticles formed after incubation of αS containing glial inclusions purified from diseased brain tissue and treated with mild detergents (Figure 13).

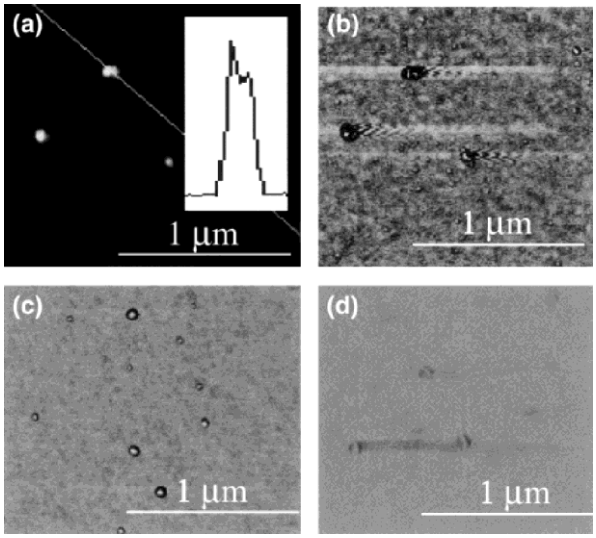

Figure 13 – AFM (a) height and (b – d) phase images of detergent-treated glial cytoplasmic inclusions, displaying annular nanoparticles. (a, b) Anti-αS conjugated probe, with inset, height cross-section of individual particle. (b) Corresponding phase image, showing a strong phase response to indicate presence of αS. (c) Anti-SUMO-1 antibody-functionalized probe (phase image). (d) Bovine serum albumin-functionalized probe (phase image). Adapted with permission from [185].

Control experiments using probes modified with antibodies not found in the sample showed significantly smaller phase signals than using the anti-αS antibody-functionalized probe. Further controls to remove any phase effects due to tip morphology variations, such as a system in which multiple proteins are present on the same surface or introduction of free antibody/protein to block molecular recognition, would further confirm αS recognition.
More recently, Chen *et al.*[186] determined that incubation of αS with D-ribose resulted in significantly increased aggregation. The resulting aggregates were 20 nm high. When their frequency increased, fibril formation was inhibited. Fibril formation was also inhibited by the addition of hydroquinone and dopamine, as demonstrated by means of AFM by Li *et al.*[187]. However, small spherical αS oligomers were still observed after incubation with these compounds, suggesting that the fibril formation is inhibited due to stabilization of pre-fibril structures. Indeed, Hong *et al.*[188] made similar observations when incubating αS with hydroquinone and nicotine, which resulted in greatly reduced fibril formation by stabilizing three types of small oligomer, with heights 16, 10 and 4 nm. Whilst Li *et al.* argued for a mechanism involving dopamine driven stabilization of αS oligomers in the brain, Hong *et al.* claimed that compounds in cigarette smoke have potential as a treatment to prevent αS plaque formation in Parkinson's disease for a similar reason. However, given the recent spur of research strongly suggesting that αS oligomers are toxic [180,181,189], cigarette smoke may actually be contraindicated in Parkinson's disease.
Similar to αS, research into the oligomeric or pre-fibrillar structure of PrP^{SC}, as seen with other amyloidic aggregations, also suggests a toxic intermediate prior to fibril formation. Silveira *et al.*[190] showed that the most infectious PrP^{SC} aggregates are composed of only 14 – 28 molecules, with molecular weights of 300 – 600 kDa and an outer diameter of 17 – 27 nm.
In general, PrP aggregation literature focuses on the infectious nature of prion disease, with less emphasis on research on the toxicity mechanism. Some research suggests that it is the pre-fibrillar structures that should be the focus of therapeutic interventions to prevent cytotoxicity of neural cells [191,192], although investigations into dismantling the amyloidic fibers are undoubtedly also important for treatment of brain tissue inclusions [193] and are also highly infectious. The interested reader is referred to further work on the topic of the toxicity and infectivity of amyloid species [139,162,181,189,191,192,194,195].

2.3 Molecular Recognition of Protein Fibers

Although the nanomechanical investigative powers of AFM have been utilized for amyloid fibril investigations [196, 197], one interesting capability of AFM has been overlooked: The use of molecular recognition on amyloid fibers seems to be absent from the literature. However, some interesting applications of TREC to non-amyloid fibers from the literature will be described in the following.

Chtcheglova *et al*.[95,198] functionalized an AFM probe with vascular endothelial-cadherin antibody fragments and performed TREC on endothelial mouse cells. Recognition was observed, as seen in Figure 14 below, primarily along the actin filaments on the cell surface. The cells were treated with glutaraldehyde to make the cell surface stiffer, and with nocodazole to depolymerise microtubules, hence actin filaments were easily observed on the cell surface.

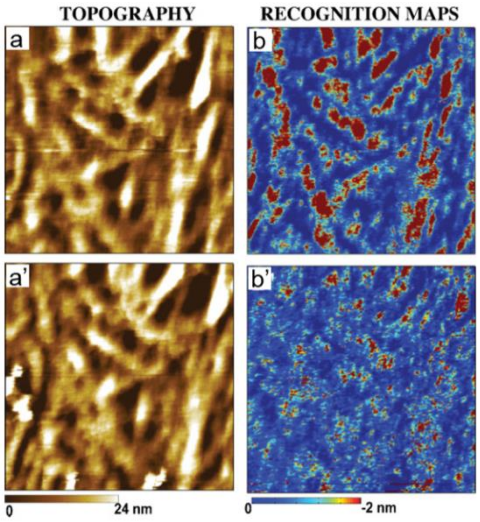

Figure 14- TREC AFM images acquired on a mouse endothelial cell surface treated with 50 μM of nocodazole for 80 minutes and subsequently fixed with glutaraldehyde, displaying topography (a, z-scale = 24 nm) and recognition images (b, z-scale = 2 nm). After addition of 5 mM EDTA in the fluid cell, the recognition spots (dark red domains) were reduced (b'). Blocking experiments did not affect the membrane topography (a'). Adapted with permission from [198].

Recognition was shown to occur via a calcium-mediated dimerisation of vascular endothelial-cadherin, and could be blocked via the addition of ethylenediaminetetraacetic acid (EDTA) to remove free calcium ions (Figure 14 B).

Creasey *et al*.[75] have taken TREC from the cellular level to the analysis of tissue. Recognition of the chaperone protein clusterin was detected on human lens capsules from patients undergoing cataract surgery. The recognition images generated were then compared to lens capsule samples affected by the protein aggregation disease Pseudoexfoliation Syndrome (PEX) [75, 199]. Recognition was only observed in small, localized areas on the normal lens capsule surfaces. In contrast, larger, localized fibers of clusterin were observed on the PEX affected lens capsules (Figure 15).

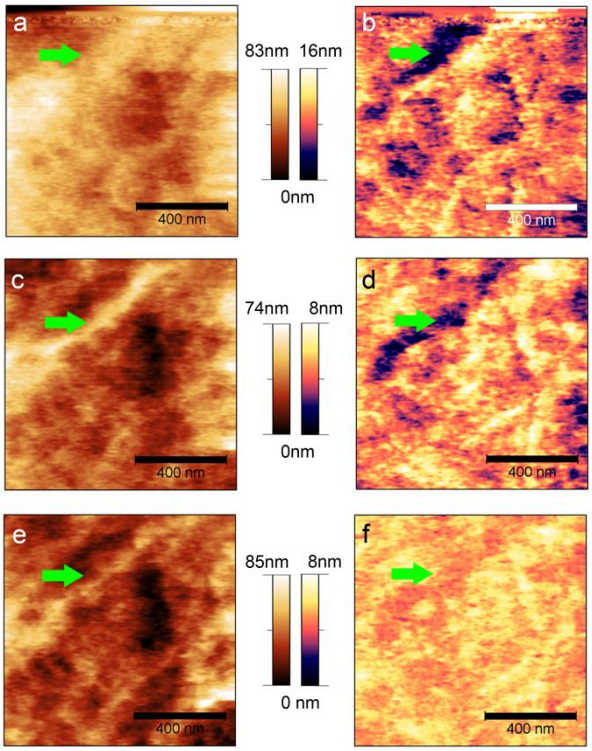

Figure 15 – TREC AFM images detecting clusterin on a PEX-affected lens capsule, displaying topography (left) and recognition (right). The arrows indicate a topographical feature and the corresponding recognition feature. (a and b) are acquired with a tip oscillation amplitude of 15 nm, (c and d) with 30 nm, and (e and f)with 45 nm. These amplitude variations are a method for confirming specificity of recognition. Scale bars = 400 nm. Adapted with permission from [75].

Immunofluorescence imaging was used to validate the presence of the larger clusterin patches on PEX affected lens capsules in comparison to normal capsules. This study was then extended to lysyl oxidase-like 1 (LOXL1) protein on PEX affected lens capsules [199] where recognition was observed on the fibers seen on the PEX affected capsule surface. The presence of LOXL1 seen by TREC was validated by means of force spectroscopy, followed by a comparison of force-volume and phase imaging with TREC. For these tissue samples, TREC was found to be the most appropriate technique due to the high resolution and robust specificity proof methodology. Such studies may assist in the elucidation of PEX pathophysiology [200 – 202].

2.4 Synthetic Fiber-Forming Peptides

Natural systems such as cells have been successfully building nanostructures since the beginning of life. Therefore, it makes sense to research and emulate the bottom-up construction employed by nature. The study of self-assembling systems and biological nanostructures is critical for nano- and biomaterial research [203]. In particular, fiber-forming molecules are receiving increased attention for use in cell scaffolds, biosensors, bio-reactive materials, and as nanowires [130,204-206]. There has been an explosion of research exploiting synthetic peptide molecules resulting in fiber formation [130,204,207] and 3D gel scaffolds [208,209]. The adsorption of peptide fiber solution to a flat surface allows morphological analysis by AFM under a variety of conditions, not only as an endpoint but also during the self-assembly process. AFM is an ideal method for the analysis of fibrous nanomaterials due to the low interaction forces leading to sensitive mechanical measurements [196], and the high resolution of the technique affording important structural information [10].

The laboratory of Shuguang Zhang [203, 204] has focused on ionic self-complementary peptides to form amyloid nanofibers. Following observations of the rapid and stable self-assembly of a lysine, phenylalanine and glutamic acid-based peptide sequence (FKFEFKFE) [210], AFM revealed the helical structure of KFE8 peptide oligomers as seen in Figure 16(a) below [211]. Using a combination of AFM, CD spectroscopy, and molecular modeling, β-sheet formation of protofibrils and fibrils over time was deduced.

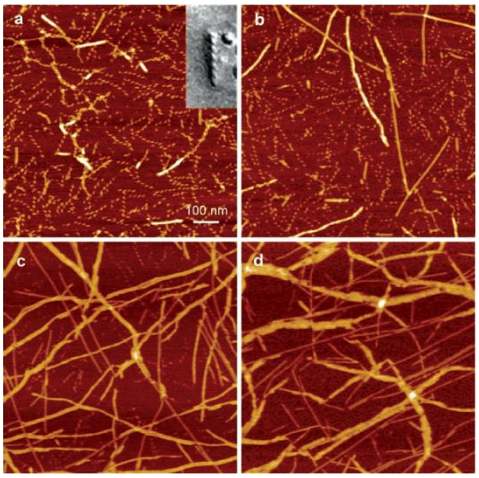

Figure 16 – AFM height images of the self-assembly of KFE8 peptide in aqueous solution (a) 8 min (Inset: EM image of a sample of peptide solution obtained using the quick-freeze deep-etch technique), (b), 35 min (c), 2 h and (d), 30 h after preparation. Scale bar = 100 nm. Adapted with permission from [211].

The helical oligomers observed at shorter timeframes decreased in frequency after ~2 hours, being replaced instead with smooth protofibrils of ~8 nm height, which then bundled together to form fibrils of increasing thickness but similar length. During these experiments, the authors made an effort to eliminate artifacts that can affect the assembly of the peptides—including sample-substrate interactions—by observing fibril formation on three different substrates, and by rinsing the adsorbed peptide aggregates with pure water before drying for imaging. Zhang and Luo *et al.*[212] studied the aggregation of alanine and glycine-based 'two-tail' peptides, containing a hydrophilic center and two hydrophobic 'tails'. These peptides were denoted 'AXG', where the X was replaced with aspartic acid, lysine or arginine. The effect of peptide concentration, temperature, ionic strength and buffer pH was studied. In the absence of salt, peptide aggregation was not observed by AFM, despite DLS showing a wide size range of nanoparticles (100 – 800 nm) in solution. By adding NaCl or upon incubation in phosphate buffered saline, superstructures such as nano-layer networks and nanofibers were observed by AFM, while CD spectroscopy indicated a reduction in β-sheet structure in the peptide secondary structure. The authors posit that more experiments are required to understand the relation between the primary structure of two-tail peptides and their aggregation properties under various environment conditions, and thus do not fully reconcile the CD spectroscopy and AFM results.

The effect of temperature on peptide self-assembly was studied by Tiné *et al.*[213] using an arginine, tryptophan and aspartic acid –based peptide sequence (RWDW). AFM revealed a dense entanglement of fibers at lower temperatures (15°C and 25°C), whilst the physiologically relevant results acquired at 35°C incubation revealed distinct, shorter protofibrils along with round aggregates. These results were interpreted in terms of changes in enthalpy of peptide aggregation as determined by isothermal titration calorimetry and differential scanning calorimetry.

Hydrogels formed by highly networked fibers can ideally be applied as a tissue engineering scaffold. Studying an arginine, alanine and aspartic acid-based peptide (RADA-16), Zhang and Yokoi *et al.*[214] observed the assembly and disassembly of nanofibers scaffolds. The RADA-16 peptides aggregated to form a hydrogel immediately in aqueous solution which consisted of fibers ranging from 100 nm to several microns lengths. By sonicating the self-assembled hydrogel, the peptide building blocks could be disassembled. Over a time period of only 2 minutes, short fibers of 20 – 100 nm length were observed by the AFM, elongating to their pre-sonication length of over 100 nm after 2 hours of incubation. A further observation from the AFM images was that the order of packing seen upon reassembly had a more ordered overall structure than the initial assembly. This assembly and disassembly cycle could be repeated multiple times on the same sample, showing the repeatability and durability of the peptide assembly process for use as a dynamic tissue engineering scaffold as well as adding interesting insights to the formation of and resistance to treatment of amyloid protein based diseases.

Likewise, Zhang and Luo *et al.*[215] investigated nanofiber formation of a glutamic acid, alanine and lysine–based peptide (EAK-16) for use as a scaffold. The formation of nanofibers of 10 nm height was observed by TM AFM in air on mica. Using CD, the secondary structure of these fibers at neutral pH was shown to be primarily β-sheet. At very low or high pH, fibers were not readily observed and the secondary structure changed from β-sheet to α-helix. The authors also observed that L-amino acid-based peptide assemblies resisted protease degradation, while the corresponding D-amino acid-based peptide assemblies were more stable at high temperatures. Considering the otherwise identical nature of opposite chirality peptide sequences, this may reflect a slight difference in inter-molecular bonding based on the chirality of amino acid residues. The stability of scaffolds for tissue engineering could therefore be manipulated using the stereochemistry of the peptide building

blocks. Indeed, Sun and Zheng [216] investigated a lysine, leucine and aspartic acid-based (KLD-12) peptide sequence for use as an injectable cell scaffold. In pure water, KLD-12 existed in monomeric form. However, self-assembly into a hydrogel composed of thin, anfractuous, highly networked nanofibers was triggered by introducing salt [217]. The authors suggested that the assembly of KLD-12 occurred via β-sheet interactions. However, no spectroscopic method was used to confirm this. An aqueous solution KLD-12 was used for injection into a mesenchymal stem cell culture, where the physiologically relevant ionic strength of the cell media caused the formation of the gel, encapsulating stem cells to create a 3D scaffold.
Wang *et al.*[218] formed fibers from random coil peptides based on an alanine, glutamic acid, tyrosine and lysine-based sequence (AEAEYAKAK), which formed dense, directional fibers (Figure 17) formed by a 'Lego-type assembly'. No characteristic ordered secondary structure motif was identified in the assembled fibers.

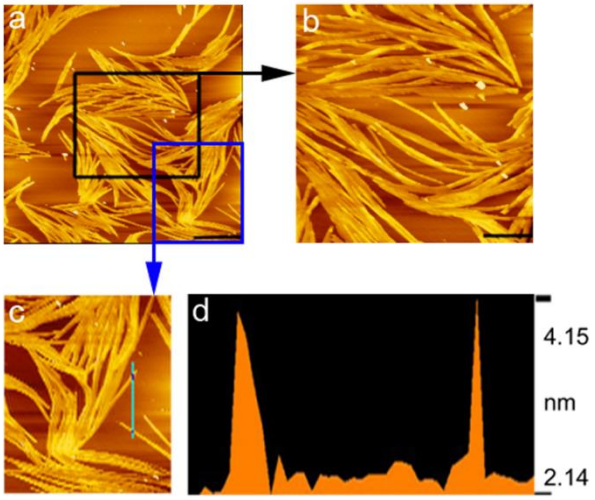

Figure 17 – AFM height image of peptides deposited on mica (a, x-scale = 2 μm). (b, c) Higher magnification of (a) (x-scale = 1 μm). (d) Line profile through the directional fibers as noted in (c), indicating a height of approximately 2.1 nm. Adapted from [218].

Kogan *et al.*[219] investigated fiber formation of peptides based on the maize storage protein, γ-zein. The valine, histidine, leucine, and proline sequence (VHLPPP) resulted in polyproline II helices, which then assembled into long nanorods when placed on a hydrophobic surface. The self-assembly process involved micellar aggregation in aqueous solution as confirmed by X-ray scattering and TEM [220]. Unfortunately, the authors did not study the effect of the wettability of the underlying substrate surface.
Synthesized peptide sequences are the first step to designer biomaterials. Arguably, an important next step is the design of novel peptide-based molecules. A class of highly branched macromolecules, called dendrimers, is one way of combining the biological relevance of amino acids and the tunability of synthetic chemistry [208,221]. Dendrimers are of particular interest due to the definition of functional motifs on the surface combined with tunability of mass and size in a monodisperse manner [222,223].
Haridas *et al.*[224] synthesized lysine-based peptide dendrons and dendrimers and studied their assembly into fibers and gels by means of AFM. The symmetrical 2nd and 3rd generation dendrons formed vesicles in organic solution, which coalesced into a dense network of fibers upon addition of a non-solvent, persisting in aqueous buffer. Self-assembling diacetylene-core dendrimers were also prepared which could be crosslinked under UV irradiation as seen in Figure 18.

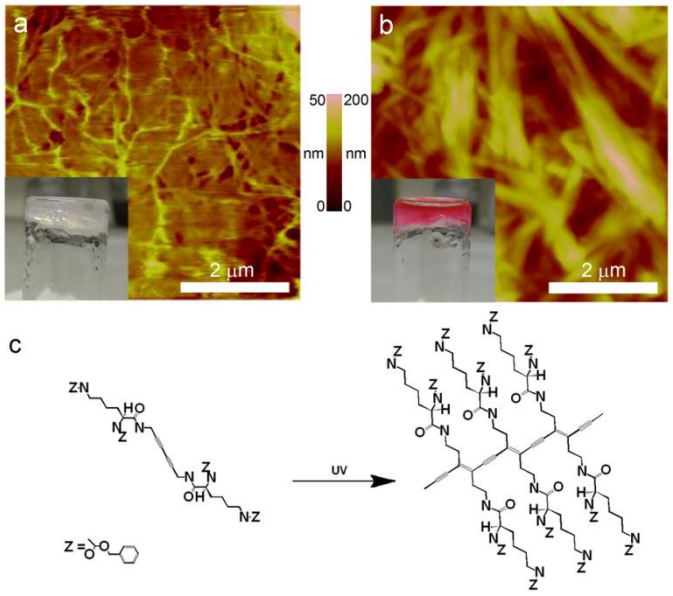

Figure 18 - Height mode TM AFM images of a gel of dendrimer **5a** (a) before and (b) after irradiation with an Hg Lamp. The insets shown in (a, b) show photographs of the respective gels in inverted tubes. (c) Structure of **5a** before and after UV irradiation. Adapted from [224].

The supramolecular organization of peptide-based synthetic chemicals such as dendrimers can be exploited to form fibrous hydrogels for drug delivery, tissue engineering scaffolds, biosensors, and novel biomaterials [222,225,226].

Biologically inspired peptide self-assemblies with a wide range of envisioned applications are constantly being developed, with the AFM being the critical tool for characterization of the resulting nanostructures [227] such as nanobelts [228] and nanotubes [229,230]. This review focused on the most recent or critical developments in fiber forming peptides investigated by AFM and left aside a plethora of interesting work on other structural elements.

3. Conclusions and Future Perspectives

The AFM is a scanning probe technique, capable of 'feeling' the 3D topography of surfaces at the nanoscale, as well as affording information on the nanomechanical and compositional properties of a range of samples. Due to its ability to perform experiments in a physiological environment without special sample preparation, AFM is perfectly suited for biological investigations. In this review, AFM operating conditions and modes were described with particular relevance to the investigation of proteins and their aggregates. Methodologies for molecular recognition mapping using the AFM including force-volume imaging and TREC were also highlighted. These techniques have strong potential for the nanoscale compositional analysis of biological samples.

In the second part of the review, recent and key examples of using AFM for the characterization of amyloid fibers were highlighted. The AFM is able to structurally characterize the polymorphisms of fibers, indicating potential pathways of aggregation. In concert with techniques such as fluorescence microscopy, EM, and spectroscopic tools such as CD spectroscopy, basic mechanisms of aggregation are being elucidated. Time-lapse AFM can be used to investigate kinetics of fiber growth, and the effects of environmental conditions, seeding, and choice of substrate surface can be parsed out. Oligomers have been identified as an integral part of amyloidosis, potentially forming the cytotoxic species of diseases such as Alzheimer's and Parkinson's. TREC was shown to be an effective molecular recognition imaging technique on cells and tissues for detection of fibers in physiological environments.

Research on synthetic fiber-forming peptides where the AFM underpinned the investigation into the structural properties of self-assembling fibers and fiber networks were subsequently reviewed. Peptide self-assembly was seen to occur for β-sheet, α-helix and polyproline II secondary structures, and peptide fibers used as scaffolds for tissue engineering and as drug delivery vehicles. Unique morphologies and self-assembly mechanisms were designed and AFM used as the main tool to explore the resulting structures.

In terms of future perspectives, it is clear that the AFM based investigation of fiber-forming proteins has key applications in drug discovery, particularly where the morphological and toxicological characterization of amyloid aggregates can be used to identify therapeutic targets, to investigate the influence of environmental factors on amyloid aggregation, and to study the efficacy of therapeutic drugs designed to disrupt aggregates. At the same

time, AFM analysis underpins the design of novel peptide-based fiber forming molecules for applications in tissue engineering scaffolds and drug delivery.
The potential of AFM-based antibody-recognition imaging has thus far been underutilized, and we foresee the use of this high-resolution technology for discovering the pathogenesis of protein aggregation diseases such as Alzheimer's and PEX syndrome. Further advances in AFM technology including high speed scanners or high throughput AFM have not been reviewed here, but these advances will no doubt have a bearing on the implementation of molecular recognition imaging.
In summary, the AFM is an invaluable asset to the life scientist interested in the studying the fascinating phenomenon of protein aggregation.

Acknowledgements
The authors acknowledge National Health & Medical Research Centre of Australia for financial assistance and Elise Ruthenbeck for proofreading.

References

[1] Binnig, G. Quate, C.; Gerber, C. Atomic force microscope. *Phys. Rev. Lett.* **1986**.

[2] Morris, V. J. Kirby, A. R.; Gunning, A. P. *Atomic force microscopy for biologists*; 2nd ed. Imperial College Press: London, **2009**.

[3] Hansma, H.; Hoh, J. Biomolecular imaging with the atomic force microscope. *Annu. Rev. Biophys. Biomol. Struct.* **1994**, *23*, 115-39.

[4] Firtel, M.; Beveridge, T. J. Scanning probe microscopy in microbiology. *Micron*, **1995**, *26*, 347-62.

[5] Müller, D. J.; Dufrêne, Y. F. Atomic force microscopy as a multifunctional molecular toolbox in nanobiotechnology. *Nat. Nanotechnol.* **2008**, *3*, 261-9.

[6] Cohen, S.; Bitler, A. Use of AFM in bio-related systems. *Curr. Opin. Colloid Interface Sci.* **2008**, *13*, 316-325.

[7] Francis, L. W. Lewis, P. D. Wright, C. J.; Conlan, R. S. Atomic force microscopy comes of age. *Biol. Cell.* **2010**, *102*, 133-43.

[8] Santos, N. C.; Castanho, M. R. B. An overview of the biophysical applications of atomic force microscopy. *Biophys. Chem.* **2004**, *107*, 133-49.

[9] Hansma, H.; Pietrasanta, L. Atomic force microscopy and other scanning probe microscopies. *Curr. Opin. Chem. Biol.* **1998**, 579-584.

[10] Silva, L. P. Imaging proteins with atomic force microscopy: an overview. *Curr. Protein Pept. Sci.* **2005**, *6*, 387-95.

[11] Ascoli, C. Normal and lateral forces in scanning force microscopy. *J. Vac. Sci. Technol. B Microelectron Nanometer Struct. Process Meas. Phenom.* **1994**, *12*, 1642.

[12] García, R. Dynamic atomic force microscopy methods. *Surf. Sci.Rep.***2002**, *47*, 197-301.

[13] Putman, C. Werf, K. V. der; Grooth, B. G. D. Hulst, N. F. V.; Greve, J. Tapping mode atomic force microscopy in liquid. *Appl. Phys. Lett.* **1994**, *64*, 2454-2456.

[14] Magonov, S. N. Elings, V.; Whangbo, M.-H. Phase imaging and stiffness in tapping-mode atomic force microscopy. *Surf. Sci.* **1997**, *375*, L385-L391.

[15] Tamayo, J.; Garcı, R. Relationship between phase shift and energy dissipation in tapping-mode scanning force microscopy. *Appl. Phys. Lett.* **1998**, *73*, 2926-2928.

[16] Giessibl, F. J. Atomic resolution of the silicon (111)-(7x7) surface by atomic force microscopy. *Science* **1995**, *267*, 68-71.

[17] Giessibl, F. J. Advances in atomic force microscopy. *Rev. Mod. Phys.* **2003**, *75*, 949-983.

[18] Dammer, U. Hegner, M. Anselmetti, D. Wagner, P. Dreier, M. Huber, W.; Güntherodt, H. J. Specific antigen/antibody interactions measured by force microscopy. *Biophys. J.* **1996**, *70*, 2437-41.

[19] Alessandrini, A.; Facci, P. AFM: a versatile tool in biophysics. *Meas. Sci. Technol.* **2005**, *16*, R65-R92.

[20] Tansock, J.; Williams, C. Force measurement with a piezoelectric cantilever in a scanning force microscope. *Ultramicroscopy* **1992**, *42-44*, 1464-1469.

[21] Cappella, B.; Dietler, G. Force-distance curves by atomic force microscopy. *Surf. Sci. Rep.* **1999**, *34*, 1-104.

[22] Bhushan, B. Israelachvili, J. N.; Landman, U. Nanotribology: friction, wear and lubrication at the atomic scale. *Nature* **1995**, *374*, 607-616.

[23] Gibson, C. T. Watson, G. S.; Myhra, S. Determination of the spring constants of probes for force microscopy/spectroscopy. *Nanotechnology* **1996**, *7*, 259-262.

[24] Gibson, C. T. Watson, G. S.; Myhra, S. Scanning force microscopy-calibrative procedures for "best practice."*Scanning* **2006**, *19*, 564-581.

[25] Zlatanova, J. Lindsay, S. M.; Leuba, S. H. Single molecule force spectroscopy in biology using the atomic force microscope. *Prog. Biophys. Mol. Biol.***2000**, *74*, 37-61.

[26] Muller, V. Derjaguin, B.; Toporov, Y. P. On two methods of calculation of the force of sticking of an elastic sphere to a rigid plane. *Colloids Surf.***1983**, *7*, 251-259.

[27] Derjaguin, B. V. Muller, V. M.; Toporov, Y. P. Effect of contact deformations on the adhesion of particles. *J. Colloid Interface Sci.***1975**, *53*, 314-326.

[28] Johnson, K. L. Kendall, K.; Roberts, A. D. Surface Energy and the Contact of Elastic Solids. *Proc. R. Soc. Lond. A Math. Phys. Sci.***1971**, *324*, 301-313.

[29] Butt, H. Cappella, B.; Kappl, M. Force measurements with the atomic force microscope: Technique, interpretation and applications. *Surf. Sci. Rep.* **2005**, *59*, 1-152.

[30] Radmacher, M. Measuring the elastic properties of biological samples with the AFM. *IEEE Eng. Med. Biol. Mag.***1997**, *16*, 47–57.

[31] Cleveland, J. P. Manne, S. Bocek, D.; Hansma, P. K. A nondestructive method for determining the spring constant of cantilevers for scanning force microscopy. *Rev. Sci. Instrum.* **1993**, *64*, 403.

[32] Hutter, J. L.; Bechhoefer, J. Calibration of atomic-force microscope tips. *Rev. Sci. Instrum.* **1993**, *64*, 1868.

[33] Burnham, N., Chen, X. Hodges, C. S. Matei, G., Thoreson, E. J. Roberts, C. J. Davies, M. C.; Tendler, S. J. B. Comparison of calibration methods for atomic-force microscopy cantilevers. *Nanotechnology* **2003**, *14*, 1-6.

[34] Sader, J. E. Chon, J. W. M.; Mulvaney, P. Calibration of rectangular atomic force microscope cantilevers. *Rev. Sci. Instrum.* **1999**, *70*, 3967.

[35] Munz, M. Force calibration in lateral force microscopy: a review of the experimental methods. *J. Phys. D. Appl. Phys.***2010**, *43*, 063001.

[36] Cumpson, P. Clifford, C.; Portoles, J. Cantilever Spring-Constant Calibration in Atomic Force Microscopy. *Probe Methods VIII* **2008**.

[37] Ebner, A. Wildling, L. Zhu, R. Rankl, C.; T Functionalization of probe tips and supports for single-molecule recognition force microscopy. *STM and AFM Studies* **2008**.

[38] Chen, G. Ning, X. Park, B. Boons, G.J., Xu, B. Simple, clickable protocol for atomic force microscopy tip modification and its application for trace ricin detection by recognition imaging. *Langmuir* **2009**, *25*, 2860-4.

[39] Kamruzzahan, A. Ebner, A. Wildling, L. Kienberger, F. Riener, C. K. Hahn, C. D. Pollheimer, P. D. Winklehner, P. Hölzl, M. Lackner, B.; others Antibody linking to atomic force microscope tips via disulfide bond formation. *Bioconjug. Chem.* **2006**, *17*, 1473–1481.

[40] Ebner, A. Hinterdorfer, P.; Gruber, H. Comparison of different aminofunctionalization strategies for attachment of single antibodies to AFM cantilevers. *Ultramicroscopy* **2007**, *107*, 922-927.

[41] Barattin, R.; Voyer, N. Chemical modifications of AFM tips for the study of molecular recognition events. *Chem. Commun.***2008**.

[42] Clausen-Schaumann, H. Seitz, M. Krautbauer, R.; Gaub, H. E. Force spectroscopy with single bio-molecules. *Curr. Opin. Chem. Biol.* **2000**, *4*, 524–530.

[43] Heymann, B.; Grubmüller, H. Dynamic force spectroscopy of molecular adhesion bonds. *Phys. Rev. Lett.***2000**, *84*, 6126-9.

[44] Lee, C. K. Wang, Y. M. Huang, L. S., Lin, S. Atomic force microscopy: determination of unbinding force, off rate and energy barrier for protein-ligand interaction. *Micron* **2007**, *38*, 446–461.

[45] Evans, E.; Ritchie, K. Dynamic strength of molecular adhesion bonds. *Biophys. J.***1997**, *72*, 1541-55.

[46] Willemsen, O. H. Snel, M., Cambi, M., Greve, J. De Grooth, B. G.; Figdor, C. G. Biomolecular interactions measured by atomic force microscopy. *Biophys. J.* **2000**, *79*, 3267-81.

[47] Leckband, D., Israelachvili, J. Intermolecular forces in biology. *Q. Rev. Biophys.* 2001; Vol. 34, pp. 105-267.

[48] Kienberger, F. Ebner, A. Gruber, H. J.; Hinterdorfer, P. Molecular recognition imaging and force spectroscopy of single biomolecules. *Acc. Chem. Res.* **2006**, *39*, 29-36.

[49] Hinterdorfer, P., Dufrêne, Y. F. Detection and localization of single molecular recognition events using atomic force microscopy. *Nat. Methods* **2006**, *3*, 347-55.

[50] Izrailev, S.; Stepaniants, S.; Balsera, M.; Oono, Y.; Schulten, K. Molecular dynamics study of unbinding of the avidin-biotin complex. *Biophys. J.* **1997**, 1568-1581.

[51] Ludwig, M., Dettmann, W., Gaub, H. Atomic force microscope imaging contrast based on molecular recognition. *Biophys. J.***1997**, *72*, 445-448.

[52] Chilkoti, A., Boland, T. Ratner, B. D., Stayton, P. S. The relationship between ligand-binding thermodynamics and protein-ligand interaction forces measured by atomic force microscopy. *Biophys. J.***1995**, *69*, 2125-30.

[53] Lo, Y.-shiu; Simons, J.; Beebe, T. P. Temperature Dependence of the Biotin-Avidin Bond-Rupture Force Studied by Atomic Force Microscopy. *J. Phys. Chem. B* **2002**, 9847-9852.

[54] Chen, a; Moy, V. T. Cross-linking of cell surface receptors enhances cooperativity of molecular adhesion. *Biophys. J.***2000**, *78*, 2814-20.

[55] Wong, J. Chilkoti, a; Moy, V. T. Direct force measurements of the streptavidin-biotin interaction. *Biomol. Eng.***1999**, *16*, 45-55.

[56] Grandbois, M. Beyer, M. Rief, M. Clausen-Schaumann, H.; Gaub, H. How strong is a covalent bond? *Science* **1999**, *283*, 1727-30.

[57] Langry, K. C. Ratto, T. V. Rudd, R. E.; McElfresh, M. W. The AFM measured force required to rupture the dithiolate linkage of thioctic acid to gold is less than the rupture force of a simple gold-alkyl thiolate bond. *Langmuir* **2005**, *21*, 12064-7.

[58] Ratto, T. V. Langry, K. C. Rudd, R. E. Balhorn, R. L. Allen, M. J.; McElfresh, M. W. Force spectroscopy of the double-tethered concanavalin-A mannose bond. *Biophys. J.***2004**, *86*, 2430-7.

[59] Touhami, A. Jericho, M. H.; Beveridge, T. J. Molecular recognition forces between immunoglobulin G and a surface protein adhesin on living Staphylococcus aureus. *Langmuir* **2007**, *23*, 2755-60.

[60] Riener, C. Simple test system for single molecule recognition force microscopy. *Anal. Chim. Acta.* **2003**, *479*, 59-75.

[61] Lee, H. Scherer, N. F.; Messersmith, P. B. Single-molecule mechanics of mussel adhesion. *Proc. Natl. Acad. Sci. U.S.A* **2006**, *103*, 12999-3003.

[62] Stroh, C. M., Ebner, A., Geretschläger, M., Freudenthaler, G., Kienberger, F., Kamruzzahan, S. M., Smith-Gill, S. J., Gruber, H. J.; Hinterdorfer, P. Simultaneous topography and recognition imaging using force microscopy. *Biophys. J.***2004**, *87*, 1981-90.

[63] Stroh, C. Wang, H. Bash, R. Ashcroft, B. Nelson, J. Gruber, H. Lohr, D. Lindsay, S. M.; Hinterdorfer, P. Single-molecule recognition imaging microscopy. *Proc. Natl. Acad. Sci. U.S.A* **2004**, *101*, 12503-7.

[64] Willemsen, O. H. Snel, M. M. van der Werf, K. O. de Grooth, B. G. Greve, J. Hinterdorfer, P. Gruber, H. J. Schindler, H. van Kooyk, Y.; Figdor, C. G. Simultaneous height and adhesion imaging of antibody-antigen interactions by atomic force microscopy. *Biophys. J.***1998**, *75*, 2220-8.

[65] Ebner, A. Kienberger, F. Kada, G. Stroh, C. M. Geretschläger, M. Kamruzzahan, S. M. Wildling, L. Johnson, W. T. Ashcroft, B. Nelson, J. Lindsay, S. M. Gruber, H. J.; Hinterdorfer, P. Localization of single avidin-biotin interactions using simultaneous topography and molecular recognition imaging. *ChemphyschemPC* **2005**, *6*, 897-900.

[66] Baumgartner, W. Hinterdorfer, P. Ness, W. Raab, A. Vestweber, D. Schindler, H.; Drenckhahn, D. Cadherin interaction probed by atomic force microscopy. *Proc. Natl. Acad. Sci. U.S.A* **2000**, *97*, 4005-10.

[67] Nevo, R. Stroh, C. Kienberger, F. Kaftan, D. Brumfeld, V. Elbaum, M. Reich, Z.; Hinterdorfer, P. A molecular switch between alternative conformational states in the complex of Ran and importin β1. *Nat. Struct. Biol.***2003**, *10*, 553-557.

[68] Wieland, J., Gewirth, A., Leckband, D. E. Single molecule adhesion measurements reveal two homophilic neural cell adhesion molecule bonds with mechanically distinct properties. *J. Biol. Chem.***2005**, *280*, 41037-46.

[69] Etienne, M.; Walcarius, A. Analytical investigation of the chemical reactivity and stability of aminopropyl-grafted silica in aqueous medium. *Talanta* **2003**, *59*, 1173-88.

[70] Moon, J. H. Shin, J. W. Kim, S. Y.; Park, J. W. Formation of Uniform Aminosilane Thin Layers : An Imine Formation To Measure Relative Surface Density of the Amine Group. *Langmuir* **1996**, *7463*, 4621-4624.

[71] Flink, S. van Veggel, F. C. J. M.; Reinhoudt, D. N. Functionalization of self-assembled monolayers on glass and oxidized silicon wafers by surface reactions. *J. Phys. Org. Chem.* **2001**, *14*, 407-415.

[72] Lyubchenko, Y. Shlyakhtenko, L. Harrington, R.; Odent, P. Atomic force microscopy of long DNA : Imaging in air and under water. *Proc. Natl. Acad. Sci. USA* **1993**, *90*, 2137-2140.

[73] Bergkvist, M. Carlsson, J. Karlsson, T.; Oscarsson, S. TM-AFM Threshold Analysis of Macromolecular Orientation: A Study of the Orientation of IgG and IgE on Mica Surfaces. *J. Colloid Interface Sci.***1998**, *206*, 475-481.

[74] Chtcheglova, L. a; Wildling, L. Waschke, J. Drenckhahn, D.; Hinterdorfer, P. AFM functional imaging on vascular endothelial cells. *J. Mol. Recognit.***2010**, *23*, 589-96.

[75] Creasey, R. Sharma, S. Craig, J. E. Gibson, C. T. Ebner, A. Hinterdorfer, P.; Voelcker, N. H. Detecting protein aggregates on untreated human tissue samples by atomic force microscopy recognition imaging. *Biophys. J.***2010**, *99*, 1660-7.

[76] Lee, S.; Chemical functionalization of AFM cantilevers. Masters Thesis, Massachusetts Institute of Technology: USA **2005**.

[77] Bergkvist, M.; Cady, N. C. Chemical functionalization and bioconjugation strategies for atomic force microscope cantilevers. In *Methods in Mol Biol (Clifton, N.J.)*; Mark, S. S., Ed. Humana Press: Totowa, NJ, **2011**; Vol. 751, 381-400.

[78] Grütter, P. Zimmermann-Edling, W.; Brodbeck, D. Tip artifacts of microfabricated force sensors for atomic force microscopy. *Appl Phys Lett.* **1992**, *60*, 2741.

[79] Niedermann, P. Hänni, W. Morel, D. Perret,; Skinner, N. Indermühle, P.F., de Rooij, N.-F.; Buffat, P.-A. CVD diamond probes for nanotechnology. *Appl. Phys. A. Mater. Sci. Process.* **1998**, *66*, 31-34.

[80] Hafner, J. H. Cheung, C. L. Woolley, T.; Lieber, C. M. Structural and functional imaging with carbon nanotube AFM probes. *Prog. Biophys. Mol. Biol.* **2001**, *77*, 73-110.

[81] Ge, G. Han, D. Lin, D. Chu, W. Sun, Y. Jiang, L. Ma, W.; Wang, C. MAC mode atomic force microscopy studies of living samples, ranging from cells to fresh tissue. *Ultramicroscopy* **2007**, *107*, 299–307.

[82] Kumar, S.; Li, M. S. Biomolecules under mechanical force. *Phys. Rep.***2010**, *486*, 1-74.

[83] Sikora, A.; Bednarz, L. Direct measurement and control of peak tapping forces in atomic force microscopy for improved height measurements. *Meas. Sci. Technol.***2011**, *22*, 094005.

[84] Yacoot, A. Koenders, L.; Wolff, H. An atomic force microscope for the study of the effects of tip–sample interactions on dimensional metrology. *Meas. Sci. Technol.***2007**, *18*, 350-359.

[85] Keller, D. Reconstruction of STM and AFM images distorted by finite-size tips. *Surf. Sci.***1991**, *253*, 353-364.

[86] Relini, A. Rolandi, R. Bolognesi, M. Aboudan, M. Merlini, G. Bellotti, V.; Gliozzi, A. Ultrastructural organization of ex vivo amyloid fibrils formed by the apolipoprotein A-I Leu174Ser variant: an atomic force microscopy study. *Biochim. Biophys. Acta* **2004**, *1690*, 33-41.

[87] Bykov, V. Gologanov, A; Shevyakov, V. Test structure for SPM tip shape deconvolution. *Appl Phys A Mater Sci Process* **1998**, *66*, 499-502.

[88] Noy, A. Vezenov, D. V.; Lieber, C. M. Chemical force microscopy. *Annual. Rev. Mat. Sci*.**1997**, *27*, 381–421.

[89] Frisbie, C. D. Rozsnyai, L. F. Noy, A. Wrighton, M. S.; Lieber, C. M. Functional group imaging by chemical force microscopy. *Science* **1994**, *265*, 2071-4.

[90] Ye, Z.; Zhao, X. Phase imaging atomic force microscopy in the characterization of biomaterials. *J Microsc.* **2010**, *238*, 27-35.

[91] Radmacher, M. Cleveland, J. Fritz, M. Hansma, H.; Hansma, P. Mapping interaction forces with the atomic force microscope. *Biophys. J.***1994**, *66*, 2159-2165.

[92] Johnson, W. Kada, G. Stroh, C. Gruber, H. Wang, H. Kienberger, F. Ebner, A. Lindsay, S.; Hinterdorfer, P. Simultaneous Topography and RECognition Mapping with PicoTREC™: A powerful new technology that can be used to map nanometer-scale molecular binding sites on a variety of surfaces. *NSTI-Nanotech* **2005**, *2*, 679-682.

[93] Sweers, K. van der Werf, K. Bennink, M.; Subramaniam, V. Nanomechanical properties of α-synuclein amyloid fibrils: a comparative study by nanoindentation, harmonic force microscopy, and Peakforce QNM. *Nanoscale Res. Lett.* **2011**, *6*, 270.

[94] Adamcik, J. Berquand, A.; Mezzenga, R. Single-step direct measurement of amyloid fibrils stiffness by peak force quantitative nanomechanical atomic force microscopy. *Appl. Phys. Lett.* **2011**, *98*, 193701.

[95] Ebner, A. Chtcheglova, L. Preiner, J. Tang, J. Wildling, L. Gruber, H.; Hinterdorfer, P. Simultaneous Topography and Recognition Imaging. In *Scanning Probe Microscopy in Nanoscience and Nanotechnology*; Springer, **2010**; pp. 325–362.

[96] Yu, J. Warnke, J.; Lyubchenko, Y. L. Nanoprobing of α-synuclein misfolding and aggregation with atomic force microscopy. *Nanomedicine* **2010**.

[97] Yu, J.; Lyubchenko, Y. L. Early stages for Parkinson's development: alpha-synuclein misfolding and aggregation. *J Neuroimmune Pharmacol.* **2009**, *4*, 10-6.

[98] Takahashi, H. Silberberg, Y. R. Kumeta, M. Edwardson, J. M.; Takeyasu, K. Force spectroscopy addresses fundamental problems in cell physiology. In *Microscopy: Science, Technology, Applications and Education*; 2010; pp. 478-488.

[99] Baumgartner, W. Hinterdorfer, P.; Schindler, H. Data analysis of interaction forces measured with the atomic force microscope. *Ultramicroscopy* **2000**, *82*, 85-95.

[100] Dupres, V. Menozzi, F. D. Locht, C. Clare, B. H. Abbott, N. L. Bompard, C. Raze, D.; Dufre, Y. F. Nanoscale mapping and functional analysis of individual adhesins on living bacteria. *Nat. Methods* **2005**, *2*.

[101] Gaboriaud, F. Parcha, B. S. Gee, M. L. Holden, J.; Strugnell, R. Spatially resolved force spectroscopy of bacterial surfaces using force-volume imaging. *Colloids Surf B Biointerfaces* **2008**, *62*, 206-13.

[102] Nussio, M. R. Voelcker, N. H. Sykes, M. J. Flavel, B. S. Miners, J. O.; Shapter, J. G. High resolution chemical mapping of biomimetic membranes by force volume imaging. *2008 International Conference on Nanoscience and Nanotechnology* **2008**, *Im*, 121-124.

[103] An, H. Nussio, M. R. Huson, M. G. Voelcker, N. H.; Shapter, J. G. Material Properties of Lipid Microdomains: Force-Volume Imaging Study of the Effect of Cholesterol on Lipid Microdomain Rigidity. *Biophys. J.***2010**, *99*, 834-844.

[104] Chirasatitsin, S.; Engler, A. J. Detecting cell-adhesive sites in extracellular matrix using force spectroscopy mapping. *J. Phys. Condens. Matter* **2010**, *22*, 194102.

[105] Nussio, M. R. Lowe, R. D. Voelcker, N. H. Flavel, B. S. Gibson, C. T. Sykes, M. J. Miners, J. O.; Shapter, J. G. Nanoscale structure of lipid domain boundaries. *Soft Matter* **2010**, *6*, 2193.

[106] Li, G. Xi, N.; Wang, D. H. Investigation of angiotensin II type 1 receptor by atomic force microscopy with functionalized tip. *Nanomedicine* **2005**, *1*, 306-12.

[107] Li, G. Xi, N.; Wang, D. H. Probing membrane proteins using atomic force microscopy. *J. Cell. Biochem.* **2006**, *97*, 1191-7.

[108] Preiner, J. Ebner, A. Chtcheglova, L. Zhu, R.; Hinterdorfer, P. Simultaneous topography and recognition imaging: physical aspects and optimal imaging conditions. *Nanotechnology* **2009**, *20*, 215103.

[109] Tang, J. Ebner, A. Badelt-Lichtblau, H. Völlenkle, C. Rankl, C. Kraxberger, B. Leitner, M. Wildling, L. Gruber, H. J. Sleytr, U. B. Ilk, N.; Hinterdorfer, P. Recognition imaging and highly ordered molecular templating of bacterial S-layer nanoarrays containing affinity-tags. *Nano lett.* **2008**, *8*, 4312-9.

[110] Chtcheglova, L. A. Atalar, F. Ozbek, U. Wildling, L. Ebner, A.; Hinterdorfer, P. Localization of the ergtoxin-1 receptors on the voltage sensing domain of hERG K+ channel by AFM recognition imaging. *Pflugers Arch.* **2008**, *456*, 247-54.

[111] Ebner, A. Nikova, D. Lange, T. Häberle, J. Falk, S. Dübbers, A. Bruns, R. Hinterdorfer, P. Oberleithner, H.; Schillers, H. Determination of CFTR densities in erythrocyte plasma membranes using recognition imaging. *Nanotechnology* **2008**, *19*, 384017.

[112] Pittenger, B. B. Erina, N.; Su, C. *Quantitative Mechanical Property Mapping at the Nanoscale with PeakForce QNM - Application Notes*; Veeco Instruments Inc., 2010.

[113] Rico, F. Su, C.; Scheuring, S. Mechanical mapping of single membrane proteins at submolecular resolution. *Nano lett.* **2011**, *11*, 3983-6.

[114] Mitsuoka, K. Hirai, T. Murata, K. Miyazawa, A. Kidera, A. Kimura, Y.; Fujiyoshi, Y. The structure of bacteriorhodopsin at 3.0 Å resolution based on electron crystallography: implication of the charge distribution. *J. Mol. Biol.***1999**, *286*, 861-82.

[115] Husale, S. Persson, H. H. J.; Sahin, O. DNA nanomechanics allows direct digital detection of complementary DNA and microRNA targets. *Nature* **2009**, *462*, 1075-8.

[116] Adamcik, J. Jung, J.-M. Flakowski, J. De Los Rios, P. Dietler, G.; Mezzenga, R. Understanding amyloid aggregation by statistical analysis of atomic force microscopy images. *Nat. Nanotechnol.* **2010**, *5*, 423-8.

[117] Adams, E. L.; Czymmek, K. J. The combined application of AFM and LSCM : Changing the way we look at innate immunity. *Imaging* **2007**, 68-76.

[118] Mangold, S. Harneit, K. Rohwerder, T. Claus, G.; Sand, W. Novel combination of atomic force microscopy and epifluorescence microscopy for visualization of leaching bacteria on pyrite. *Appl. Microbiol.* **2008**, *74*, 410-5.

[119] Makarava, N. Lee, C.-i; Ostapchenko, V. G.; Baskakov, I. V. Highly promiscuous nature of prion polymerization. *J. Biol. Chem.* **2007**, *282*, 36704 -36713.

[120] Duman, M. Pfleger, M. Zhu, R. Rankl, C. Chtcheglova, L. Neundlinger, I. Bozna, B. L. Mayer, B. Salio, M. Shepherd, D. Polzella, P. Moertelmaier, M. Kada, G. Ebner, A. Dieudonne, M. Schütz, G. J. Cerundolo, V. Kienberger, F.; Hinterdorfer, P. Improved localization of cellular membrane receptors using combined fluorescence microscopy and simultaneous topography and recognition imaging. *Nanotechnology* **2010**, *21*, 115504.

[121] Apetri, M. M. Maiti, N. C. Zagorski, M. G. Carey, P. R.; Anderson, V. E. Secondary structure of alpha-synuclein oligomers: characterization by raman and atomic force microscopy. *J. Mol. Biol.* **2006**, *355*, 63-71.

[122] Zhou, A. H. McEwen, G. D.; Wu, Y. Z. Combined AFM / Raman microspectroscopy for characterization of living cells in near physiological conditions. *Exposure* **2010**, 515-522.

[123] Prater, C. Kjoller, K. Cook, D. Shetty, R. Meyers, G. Reinhardt, C.; Felts, J. Nanoscale infrared spectroscopy of materials by atomic force microscopy. *Microsc Anal* **2010**, 5-8.

[124] Dobson, C. M. Protein misfolding, evolution and disease. *Trends Biochem. Sci.* **1999**, *24*, 329-32.

[125] Mitraki, A. Protein aggregation from inclusion bodies to amyloid and biomaterials. *Adv Protein Chem Struct Biol* **2010**, *79*, 89-125.

[126] Ecroyd, H.; Carver, J. A. Unraveling the mysteries of protein folding and misfolding. *IUBMB life* **2008**, *60*, 769-74.

[127] Chiti, F.; Dobson, C. M. Protein Misfolding, Functional Amyloid, and Human Disease. *Annu. Rev. Biochem.* **2006**, *75*, 333-366.

[128] Morris, A. M. Watzky, M.; Finke, R. G. Protein aggregation kinetics, mechanism, and curve-fitting: a review of the literature. *Biochim. Biophys. Acta* **2009**, *1794*, 375-97.

[129] Wang, W. Nema, S.; Teagarden, D. Protein aggregation--pathways and influencing factors. *Int. J. Pharm.***2010**, *390*, 89-99.

[130] Hamley, I. W. Peptide fibrillization. *Angew. Chem. Int. Ed. Engl.* **2007**, *46*, 8128-47.

[131] Bhak, G. Choe, Y.-J.; Paik, S. R. Mechanism of amyloidogenesis: nucleation-dependent fibrillation versus double-concerted fibrillation. *BMB reports* **2009**, *42*, 541-51.

[132] Merriam-Webster.com "Fiber" http://www.merriam-webster.com/dictionary/fiber?show=0&t=1317942787 (accessed Oct 7, **2011**).

[133] Makin, O. S.; Serpell, L. C. Structures for amyloid fibrils. *FEBS J* **2005**, *272*, 5950-61.

[134] Fändrich, M. On the structural definition of amyloid fibrils and other polypeptide aggregates. *Cell. Mol. Life Sci.* **2007**, *64*, 2066-78.

[135] Antzutkin, O. N. Amyloidosis of Alzheimer's Abeta peptides: solid-state nuclear magnetic resonance, electron paramagnetic resonance, transmission electron microscopy, scanning transmission electron microscopy and atomic force microscopy studies. *Magn. Reson. Chem.* **2004**, *42*, 231-46.

[136] McKhann, G. Drachman, D. Folstein, M. Katzman, R. Price, D.; Stadlan, E. M. Clinical diagnosis of Alzheimer's disease. *Neurol.* **1984**, *34*, 939.

[137] Volles, M. J.; Lansbury, P. T. Zeroing in on the pathogenic form of alpha-synuclein and its mechanism of neurotoxicity in Parkinson's disease. *Biochemistry* **2003**, *42*, 7871-8.

[138] Harper, J. D. Lieber, C. M.; Lansbury Jr, P. T. Atomic force microscopic imaging of seeded fibril formation and fibril branching by the Alzheimer's disease amyloid-β protein. *Chem. Biol.* **1997**, *4*, 951-959.

[139] Quist, A. Doudevski, I. Lin, H. Azimova, R. Ng, D. Frangione, B. Kagan, B. Ghiso, J.; Lal, R. Amyloid ion channels: a common structural link for protein-misfolding disease. *Proc. Natl. Acad. Sci. U.S.A***2005**, *102*, 10427-32.

[140] Conway, K. Lee, S.-Jae; Rochet, J.-Christophe; Ding, T.; Williamson, R. Acceleration of oligomerization, not fibrillization, is a shared property of both a-synuclein mutations linked to early-onset Parkinson's disease: Implications for pathogenesis and therapy. *Proc. Natl Acad. Sci. USA* **2000**, *99*, 571–576.

[141] Hoyer, W. Cherny, D. Subramaniam, V.; Jovin, T. M. Rapid self-assembly of alpha-synuclein observed by in situ atomic force microscopy. *J. Mol. Biol.***2004**, *340*, 127-39.

[142] Zhang, F. Lin, X.-J. Ji, L.-N. Du, H.-N. Tang, L. He, J.-H. Hu, J.; Hu, H.-Y. Assembly of alpha-synuclein fibrils in nanoscale studied by peptide truncation and AFM. *Biochem. Biophys. Res. Commun.* **2008**, *368*, 388-94.

[143] O'Brien, R. J.; Wong, P. C. Amyloid precursor protein processing and Alzheimer's disease. *Annu. Rev. Neurosci.* **2011**, *34*, 185-204.

[144] Fändrich, M. Schmidt, M.; Grigorieff, N. Recent progress in understanding Alzheimer's β-amyloid structures. *Trends Biochem. Sci.* **2011**, *36*, 338-45.

[145] Lynn, D. G.; Meredith, S. C. Review: Model peptides and the physicochemical approach to beta-amyloids. *J. Struct. Biol.* **2000**, *130*, 153-73.

[146] Prusiner, S. B. Molecular biology of prion diseases. *Science* **1991**, *252*, 1515-22.

[147] Stewart, L. Rydzewska, L. H. M. Keogh, G. F.; Knight, R. S. G. Systematic review of therapeutic interventions in human prion disease. *Neurol.* **2008**, *70*, 1272-81.

[148] Selkoe, D. Alzheimer's disease: Genes, proteins, and therapy. *Physiol. Rev.***2001**, 741-766.

[149] Hebda, J.; Miranker, A. D. The interplay of catalysis and toxicity by amyloid intermediates on lipid bilayers: insights from type II diabetes. *Annu. Rev. Biophys.* **2009**, *38*, 125-52.

[150] Sharma, K. K.; Santhoshkumar, P. Lens aging: effects of crystallins. *Biochim. Biophys. Acta***2009**, *1790*, 1095-108.

[151] Stine, W. B. Snyder, S. W. Ladror, U. S. Wade, W. S. Miller, M. F. Perun, T. J. Holzman, T. F.; Krafft, G. The nanometer-scale structure of amyloid-beta visualized by atomic force microscopy. *J. Protein Chem.* **1996**, *15*, 193-203.

[152] Toyama, B. H.; Weissman, J. S. Amyloid structure: conformational diversity and consequences. *Annu. Rev. Biochem.* **2011**, *80*, 557-85.

[153] Perutz, M. F. Finch, J. T. Berriman, J.; Lesk, A. Amyloid fibers are water-filled nanotubes. *Proc. Natl. Acad. Sci. U.S.A* **2002**, *99*, 5591-5.

[154] Bocharova, O. V. Breydo, L. Parfenov, A. S. Salnikov, V. V.; Baskakov, I. V. In vitro conversion of full-length mammalian prion protein produces amyloid form with physical properties of PrP(Sc). *J. Mol. Biol.* **2005**, *346*, 645-59.

[155] Anderson, M. Bocharova, O. V. Makarava, N. Breydo, L. Salnikov, V. V.; Baskakov, I. V. Polymorphism and ultrastructural organization of prion protein amyloid fibrils: An insight from high resolution atomic force microscopy. *J. Mol. Biol.* **2006**, *358*, 580-96.

[156] Petty, S. Adalsteinsson, T.; Decatur, S. M. Correlations among morphology, beta-sheet stability, and molecular structure in prion peptide aggregates. *Biochemistry* **2005**, *44*, 4720-6.

[157] Podestà, A. Tiana, G. Milani, P.; Manno, M. Early events in insulin fibrillization studied by time-lapse atomic force microscopy. *Biophys. J.* **2006**, *90*, 589-97.

[158] Relini, A. Torrassa, S. Rolandi, R. Gliozzi, A. Rosano, C. Canale, C. Bolognesi, M. Plakoutsi, G. Bucciantini, M. Chiti, F.; Stefani, M. Monitoring the process of HypF fibrillization and liposome permeabilization by protofibrils. *J. Mol. Biol.* **2004**, *338*, 943-57.

[159] Goldsbury, C. Kistler, J. Aebi, U. Arvinte, T.; Cooper, G. J. Watching amyloid fibrils grow by time-lapse atomic force microscopy. *J. Mol. Biol.***1999**, *285*, 33-9.

[160] Goldsbury, C. Frey, P. Olivieri, V. Aebi, U.; Müller, S. a Multiple assembly pathways underlie amyloid-beta fibril polymorphisms. *J. Mol. Biol.* **2005**, *352*, 282-98.

[161] Harper, J. D. Wong, S. S. Lieber, C. M.; Lansbury, P. T. Observation of metastable beta amyloid protofibrils by atomic force microscopy. *Chem. Biol.* **1997**, *4*, 119-25.

[162] Polano, M. Bek, A. Benetti, F. Lazzarino, M.; Legname, G. Structural insights into alternate aggregated prion protein forms. *J. Mol. Biol.* **2009**, *393*, 1033-42.

[163] Sun, Y. Makarava, N. Lee, C.-I. Laksanalamai, P. Robb, F. T.; Baskakov, I. V. Conformational stability of PrP amyloid fibrils controls their smallest possible fragment size. *J. Mol. Biol.* **2008**, *376*, 1155-67.

[164] Klöhn, P.-C. Stoltze, L. Flechsig, E. Enari, M.; Weissmann, C. A quantitative, highly sensitive cell-based infectivity assay for mouse scrapie prions. *Proc. Natl. Acad. Sci. U.S.A* **2003**, *100*, 11666-71.

[165] Wegmann, S. Miesbauer, M. Winklhofer, K. F. Tatzelt, J.; Muller, D. J. Observing fibrillar assemblies on scrapie-infected cells. *Pflugers Arch.* **2008**, *456*, 83-93.

[166] Ku, S. H.; Park, C. B. Highly accelerated self-assembly and fibrillation of prion peptides on solid surfaces. *Langmuir* **2008**, *24*, 13822-7.

[167] Ha, C.; Park, C. B. Ex situ atomic force microscopy analysis of beta-amyloid self-assembly and deposition on a synthetic template. *Langmuir* **2006**, *22*, 6977-85.

[168] Giacomelli, C. E.; Norde, W. Influence of hydrophobic Teflon particles on the structure of amyloid beta-peptide. *Biomacromolecules 4*, 1719-26.

[169] Zhu, M. Souillac, P. O. Ionescu-Zanetti, C. Carter, S.; Fink, A. L. Surface-catalyzed amyloid fibril formation. *J. Biol. Chem.***2002**, *277*, 50914-22.

[170] Kowalewski, T.; Holtzman, D. M. In situ atomic force microscopy study of Alzheimer's β-amyloid peptide on different substrates: New insights into mechanism of β-sheet formation. *Proc. Natl. Acad. Sci. U.S.A.* **1999**, *96*, 3688.

[171] Wang, Z. Zhou, C. Wang, C. Wan, L. Fang, X.; Bai, C. AFM and STM study of beta-amyloid aggregation on graphite. *Ultramicroscopy* **2003**, *97*, 73-9.

[172] Ma, X. Liu, L. Mao, X. Niu, L. Deng, K. Wu, W. Li, Y. Yang, Y.; Wang, C. Amyloid beta (1-42) folding multiplicity and single-molecule binding behavior studied with STM. *J. Mol. Biol.* **2009**, *388*, 894-901.

[173] Gorman, P. M. Yip, C. M. Fraser, P. E.; Chakrabartty, A. Alternate aggregation pathways of the Alzheimer beta-amyloid peptide: Abeta association kinetics at endosomal pH. *J. Mol. Biol.* **2003**, *325*, 743-57.

[174] Green, J. D. Kreplak, L. Goldsbury, C. Li Blatter, X. Stolz, M. Cooper, G. S. Seelig, A; Kistler, J.; Aebi, U. Atomic force microscopy reveals defects within mica supported lipid bilayers induced by the amyloidogenic human amylin peptide. *J. Mol. Biol.* **2004**, *342*, 877-87.

[175] DeMarco, M. L. Silveira, J. Caughey, B.; Daggett, V. Structural properties of prion protein protofibrils and fibrils: an experimental assessment of atomic models. *Biochemistry* **2006**, *45*, 15573-82.

[176] Krebs, M. R. H. Morozova-roche, L. A. Daniel, K. Robinson, C. V.; Dobson, C. M. Observation of sequence specificity in the seeding of protein amyloid fibrils. *Protein Sci.* **2004**, 1933-1938.

[177] Dahlgren, K. N. Manelli, A. M. Stine, W. B. Baker, L. K. Krafft, G.; LaDu, M. J. Oligomeric and fibrillar species of amyloid-beta peptides differentially affect neuronal viability. *J. Biol. Chem.***2002**, *277*, 32046-53.

[178] Zamotin, V. Gharibyan, A. Gibanova, N. V. Lavrikova, M.; Dolgikh, D.; Kirpichnikov, M. P. Kostanyan, I.; Morozova-Roche, L. Cytotoxicity of albebetin oligomers depends on cross-beta-sheet formation. *FEBS lett.* **2006**, *580*, 2451-7.

[179] Kayed, R. Sokolov, Y. Edmonds, B. McIntire, T. M. Milton, S. C. Hall, J. E.; Glabe, C. G. Permeabilization of lipid bilayers is a common conformation-dependent activity of soluble amyloid oligomers in protein misfolding diseases. *J. Biol. Chem.***2004**, *279*, 46363-6.

[180] Pountney, D. L. Voelcker, N. H.; Gai, W. P. Annular alpha-synuclein oligomers are potentially toxic agents in alpha-synucleinopathy. Hypothesis. *Neurotox. Res.***2005**, *7*, 59–67.

[181] Butterfield, S. M.; Lashuel, H. Amyloidogenic protein-membrane interactions: mechanistic insight from model systems. *Angew. Chem. Int. Ed. Engl.* **2010**, *49*, 5628-54.

[182] Lowe, R. Pountney, D. L. Jensen, P. H. Gai, W. P.; Voelcker, N. H. Calcium (II) selectively induces alpha-synuclein annular oligomers via interaction with the C-terminal domain. *Protein Sci.* **2004**, *13*, 3245–3252.

[183] Rivera-Mancía, S. Pérez-Neri, I. Ríos, C. Tristán-López, L. Rivera-Espinosa, L.; Montes, S. The transition metals copper and iron in neurodegenerative diseases. *Chem. Biol. Interact.* **2010**, *186*, 184-99.

[184] Santner, A.; Uversky, V. N. Metalloproteomics and metal toxicology of α-synuclein. *Metallomics* **2010**, *2*, 378-92.

[185] Pountney, D. L. Lowe, R. Quilty, M. Vickers, J. C. Voelcker, N. H.; Gai, W. P. Annular alpha-synuclein species from purified multiple system atrophy inclusions. *J. Neurochem.* **2004**, *90*, 502-12.

[186] Chen, L. Wei, Y. Wang, X.; He, R. Ribosylation rapidly induces alpha-synuclein to form highly cytotoxic molten globules of advanced glycation end products. *PloS One* **2010**, *5*, e9052.

[187] Li, H.-T. Lin, D.-H. Luo, X.-Y. Zhang, F. Ji, L.-N. Du, H.-N. Song, G.-Q. Hu, J. Zhou, J.-W.; Hu, H.-Y. Inhibition of alpha-synuclein fibrillization by dopamine analogs via reaction with the amino groups of alpha-synuclein. Implication for dopaminergic neurodegeneration. *FEBS J* **2005**, *272*, 3661-72.

[188] Hong, D.-P. Fink, A. L.; Uversky, V. N. Smoking and Parkinson's disease: does nicotine affect alpha-synuclein fibrillation? *Biochim. Biophys. Acta* **2009**, *1794*, 282-90.

[189] Winner, B. Jappelli, R. Maji, S. K. Desplats, P.; Boyer, L. Aigner, S. Hetzer, C. Loher, T. Vilar, M. Campioni, S. Tzitzilonis, C. Soragni, A. Jessberger, S. Mira, H. Consiglio, A. Pham, E. Masliah, E. Gage, F. H.; Riek, R. In vivo demonstration that alpha-synuclein oligomers are toxic. *Proc. Natl. Acad. Sci. U.S.A* **2011**, *108*, 4194-9.

[190] Silveira, J. R. Raymond, G. J. Hughson, A. G. Race, R. E. Sim, V. L. Caughey, B.; Hayes, S. F. The most infectious prion protein particles. *Nature* **2005**, *437*, 257.

[191] Harris, D.; True, H. L. New insights into prion structure and toxicity. *Neuron* **2006**, *50*, 353-7.

[192] Uversky, V. N. Mysterious oligomerization of the amyloidogenic proteins. *FEBS J* **2010**, *277*, 2940-2953.

[193] Dasilva, K.; Shaw, J. E.; McLaurin, J. Amyloid-beta fibrillogenesis: structural insight and therapeutic intervention. *Exp. Neurol.*. **2010**, *223*, 311-21.

[194] Lashuel, H.; Lansbury, P. T. Are amyloid diseases caused by protein aggregates that mimic bacterial pore-forming toxins? *Q. Rev. Biophys.* **2006**, *39*, 167-201.

[195] Volles, M. J.; Lansbury, P. T. Vesicle Permeabilization by Protofibrillar α-Synuclein Is Sensitive to Parkinson's Disease-Linked Mutations and Occurs by a Pore-like Mechanism. *Biochemistry* **2002**, *41*, 4595-4602.

[196] Tan, E.; Lim, C. Mechanical characterization of nanofibers – A review. *Compos Sci Technol* **2006**, *66*, 1102-1111.

[197] Meersman, F. Cabrera, R. Q. McMillan, P. F.; Dmitriev, V. Structural and mechanical properties of TTR105-115 amyloid fibrils from compression experiments. *Biophys. J* .**2011**, *100*, 193-7.

[198] Chtcheglova, L. A. Waschke, J. Wildling, L. Drenckhahn, D.; Hinterdorfer, P. Nano-scale dynamic recognition imaging on vascular endothelial cells. *Biophys. J* .**2007**, *93*, L11–L13.

[199] Creasey, R. Sharma, S. Gibson, C. T. Craig, J. E. Ebner, A. Becker, T. Hinterdorfer, P.; Voelcker, N. H. Atomic force microscopy-based antibody recognition imaging of proteins in the pathological deposits in Pseudoexfoliation Syndrome. *Ultramicroscopy* **2011**, *111*, 1055-1061.

[200] Burdon, K. P. Sharma, S. Hewitt, A. W. McMellon, A. E. Wang, J. J. Mackey, D. A. Mitchell, P.; Craig, J. E. Genetic analysis of the clusterin gene in pseudoexfoliation syndrome. *Mol. Vis.* **2008**, *14*, 1727-36.

[201] Drolsum, L. Ringvold, A.; Nicolaissen, B. Cataract and glaucoma surgery in pseudoexfoliation syndrome: a review. *Acta Ophthalmol Scand* **2007**, *85*, 810-21.

[202] Dvorak-Theobald, G. Pseudoexfoliation of the lens capsule: relation to true exfoliation of the lens capsule as reported in the literature, and role in the production of glaucoma capsulocuticulare. *Trans Am Ophthalmol Soc***1953**, *51*, 385-407.

[203] Zhang, S. Fabrication of novel biomaterials through molecular self-assembly. *Nat. Biotechnol.* **2003**, *21*, 1171-8.

[204] Hauser, C. E.; Zhang, S. Designer self-assembling peptide nanofiber biological materials. *Chem. Soc. Rev.***2010**, 2780-2790.

[205] Eichhorn, S. J. Cellulose nanowhiskers: promising materials for advanced applications. *Soft Matter* **2011**, *7*, 303.

[206] Mankar, S. Anoop,; Sen, S.; Maji, S. K. Nanomaterials: amyloids reflect their brighter side. *Nano Reviews* **2011**, *2*, 1-12.

[207] Cui, H. Webber, M. J.; Stupp, S. I. Self-assembly of peptide amphiphiles: from molecules to nanostructures to biomaterials. *Biopolymers* **2010**, *94*, 1-18.

[208] Kopecek, J.; Yang, J. Peptide-directed self-assembly of hydrogels. *Acta Biomater* **2009**, *5*, 805-16.

[209] Zhao, X. Pan, F. Xu, H. Yaseen, M. Shan, H. Hauser, C. E. Zhang, S.; Lu, J. R. Molecular self-assembly and applications of designer peptide amphiphiles. *Chem.Soc. Rev.***2010**, *39*, 3480-98.

[210] Caplan, M. R. Moore, P. N. Zhang, S. Kamm, R. D.; Lauffenburger, D. Self-assembly of a beta-sheet protein governed by relief of electrostatic repulsion relative to van der Waals attraction, *Biomacromolecules* **2000**, *1*, 627-31.

[211] Marini, D. M. Hwang, W. Lauffenburger, D. A. Zhang, S.; Kamm, R. D. Left-Handed Helical Ribbon Intermediates in the Self-Assembly of a β-Sheet Peptide. *Nano Lett.* **2002**, *2*, 295-299.

[212] Luo, Z. Åkerman, B. Zhang, S.; Nordén, B. Structures of self-assembled amphiphilic peptide-heterodimers: effects of concentration, pH, temperature and ionic strength. *Soft Matter* **2010**, *6*, 2260.

[213] Tiné, M. R. Alderighi, M. Duce, C. Ghezzi, L.; Solaro, R. Effect of temperature on self-assembly of an ionic tetrapeptide. *J Therm Anal Calorim* **2010**, *103*, 75-80.

[214] Yokoi, H. Kinoshita, T.; Zhang, S. Dynamic reassembly of peptide RADA16 nanofiber scaffold. *Proc. Natl. Acad. Sci. U.S.A***2005**, *102*, 8414-9.

[215] Luo, Z. Zhao, X.; Zhang, S. Self-organization of a chiral D-EAK16 designer peptide into a 3D nanofiber scaffold. *Macromol. Biosci.* **2008**, *8*, 785-91.

[216] Sun, J.; Zheng, Q. Experimental study on self-assembly of KLD-12 peptide hydrogel and 3-D culture of MSC encapsulated within hydrogel in vitro. *J Huazhong Univ Sci Technolog Med Sci.* **2009**, *29*, 512-6.

[217] Dai, J. Characterization of self-assembling peptide nanofibers of KLD12 and RID 12, Masters Thesis, Massachusetts Institute of Technology: USA, **2004**.

[218] Wang, L.; Zhao, X.-J. Investigation of Self-assembly Structure and Properties of a Novel Designed Lego-type Peptide with Double Amphiphilic Surfaces. *Bull. Kor. Chem. Soc.* **2010**, *31*, 3740-3744.

[219] Kogan, M. J. Dalcol, I. Gorostiza, P. López-Iglesias, C. Pons, M. Sanz, F. Ludevid, D.; Giralt, E. Self-assembly of the amphipathic helix (VHLPPP)8. A mechanism for zein protein body formation. *J. Mol. Biol.***2001**, *312*, 907-13.

[220] Kogan, M. J. Dalcol, I. Gorostiza, P. Lopez-Iglesias, C. Pons, R. Pons, M. Sanz, F.; Giralt, E. Supramolecular properties of the proline-rich gamma-Zein N-terminal domain. *Biophys. J.***2002**, *83*, 1194-204.

[221] Lee, C. C. MacKay, J.; Fréchet, J. M. J.; Szoka, F. C. Designing dendrimers for biological applications. *Nat. Biotechnol.* **2005**, *23*, 1517-26.

[222] Grinstaff, M. Dendritic macromers for hydrogel formation: Tailored materials for ophthalmic, orthopedic, and biotech applications. *J Polym Sci A Polym Chem* **2008**, *46*, 383-400.

[223] Lo, S. C. Male, N. A. H. Markham, J. P. J. Magennis, S. W. Burn, P. L. Salata, O. V.; Samuel, I. D. W. Green phosphorescent dendrimer for light-emitting diodes. *Adv. Mater.* **2002**, *14*, 975–979.

[224] Haridas, V. Sharma, Y. K. Creasey, R. Sahu, S. Gibson, C. T.; Voelcker, N. H. Gelation and topochemical polymerization of peptide dendrimers. *New Journal.Chemistry*.**2011**, *35*, 303.

[225] Hirst, A. R. Smith, D. K. Feiters, M. C. Geurts, H. P. M.; Wright, A. C. Two-component dendritic gels: easily tunable materials. *J. Am. Chem. Soc.* **2003**, *125*, 9010-1.

[226] Smith, D. K. Dendritic Gels—Many Arms Make Light Work. *Adv. Mater.* **2006**, *18*, 2773-2778.

[227] Mammadov, R. Tekinay, A. B. Dana, A.; Guler, M. O. Microscopic characterization of peptide nanostructures. *Micron* **2011**.

[228] Cui, H. Muraoka, T. Cheetham, A. G.; Stupp, S. I. Self-Assembly of Giant Peptide Nanobelts 2009. *Nano* **2009**.

[229] Ghadiri, M. Granja, J. Milligan, R.; McRee, D. Self-assembling organic nanotubes based on a cyclic peptide architecture. *Nature* **1993**.

[230] Brea, R. J. Reiriz, C.; Granja, J. R. Towards functional bionanomaterials based on self-assembling cyclic peptide nanotubes. *Chem. Soc. Rev.***2010**, *39*, 1448-56.